Regulating Intrinsic Electronic Structures of Transition-Metal-Based Catalysts and the Potential Applications for Electrocatalytic Water Splitting

Cheng-Zong Yuan[a], Kwan San Hui[b,], Hong Yin[a], Siqi Zhu[a], Jintao Zhang[c], Xi-Lin Wu[d], Xiaoting Hong[e], Wei Zhou[f], Xi Fan[g], Feng Bin[h], Fuming Chen[i,]*, Kwun Nam Hui[a,]**

[a] Joint Key Laboratory of the Ministry of Education, Institute of Applied Physics and Materials Engineering, University of Macau, Avenida da Universidade, Taipa, Macau SAR 999078, China.

[b] School of Engineering, Faculty of Science, University of East Anglia, Norwich, NR4 7TJ, United Kingdom.

[c] School of Chemistry and Chemical Engineering, Shandong University, Jinan 250061, China.

[d] College of Geography and Environmental Science, Zhejiang Normal University, Jinhua, 321004, China.

[e] Department of Chemistry, Zhejiang Sci-tech University, Hangzhou, 310018, PR China.

[f] Department of Mechanical & Electrical Engineering, Xiamen University, Xiamen 361005, China.

[g] Ningbo Institute of Materials Technology, Engineering, Chinese Academy of Sciences, Ningbo, 315201, China.

[h] State Key Laboratory of High-Temperature Gas Dynamics, Institute of Mechanics, Chinese Academy of Science, Beijing 100190, China.

[i] State Key Laboratory of Optic Information Physics and Technologies, School of Physics and Telecommunication Engineering, South China Normal University, Guangzhou, China 510006, China.

* Corresponding Author.

E-mail: k.hui@uea.ac.uk, fmchen@m.scnu.edu.cn, bizhui@um.edu.mo

Keywords: engineering strategies, transition metal electrocatalysts, electronic structure regulation, adsorption abilities, reaction barrier, water splitting

Abstract: Efficient and low-cost transition metal (TM)-based electrocatalysts have been of great importance to produce hydrogen (H_2) and oxygen (O_2) via electrocatalytic water (H_2O) splitting to ameliorate global energy and environmental problems. However, TM-based materials generally suffer from unsatisfactory electrocatalytic activity because of their relatively low conductivity and unregulated electronic structure. Therefore, electronic structure engineering on electrocatalysts is an efficient strategic approach to enhance catalytic performances and stabilities. In this review, recent experimental and theoretical advances on intrinsic electronic structure regulation of TM-based nanomaterials are summarized in terms of preparation methods and underlying natures to boost hydrogen evolution reaction (HER) and oxygen evolution reaction (OER). Systematic discussion is conducted on engineering strategies for TM-based nanomaterials to regulate their electronic structures, optimize their adsorption ability of reaction intermediates, and reduce the reaction energy barrier. The existent challenges and perspectives of TM-based electrocatalysts are highlighted to provide new insights into technological advancement for hydrogen production.

1. Introduction

The increasing demands for renewable clean energy resources and concerns of global environmental issues have attracted lots of interests in developing energy conversion and storage technologies. Among these approaches, efficient water decomposition with negligible environment pollution powered by electricity (Figure 1a) is an interesting method to produce clean hydrogen fuels,[1-3] which consists OER at the anode and HER at the cathode (shown in Figure 1b). Both of them involve multistep proton-coupled

electron transfer that is intrinsically efficiency-limited for water electrolysis.[4,5] Highly effective catalysts are always required to accelerate the catalysis rate, enhance the conversion efficiency, and reduce the overpotential of water dissociation. Until now, the most effective materials for catalyzing OER are IrO_2 and RuO_2, and the benchmark catalysts for HER are Pt group metals. However, high cost, scarcity, and instability of noble metal-based electrocatalysts seriously restrict their large-scale applications. Hence, designing and synthesizing cost-effective and efficient TM-based nanomaterials for large-scale water splitting have been an imperative yet challenging subject. Extensive efforts have been made to exploring high-efficiency OER and HER electrocatalysts based on TM elements, such as oxides, selenide, phosphides, and hydroxides for OER[6-12] and carbides, chalcogenides, nitrides, and alloys for HER.[13–18] Unfortunately, most transition metal (TM)-based catalysts have inadequate intrinsic activities compared with noble metal materials because of their relatively low conductivity and unsuitable electron structure. Electrocatalysis is always operated in harsh conditions (acidic or alkaline electrolyte) to minimize the overpotentials of water splitting. This harsh electrolyte condition poses a great challenge for most TM-based materials applied as a highly active and stable catalyst during practical application. These aspects have encouraged various engineering strategies for TM-based electrocatalysts to enhance oxygen and hydrogen evolution activity and stability.

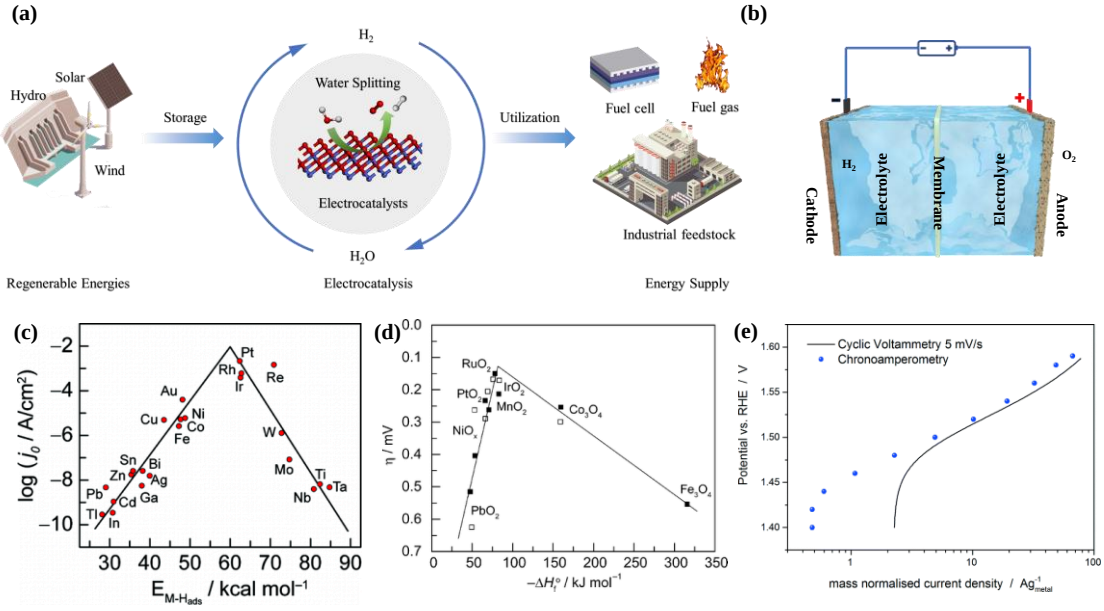

Figure 1. (a) The production and utilization cycle of H_2. (b) Schematic illustration of water electrolyzer. (c) Volcano plot of different HER metal-based electrocatalysts in acidic solution. (d) Volcano plot of OER overpotential vs. enthalpy of different metal oxides in acidic (■) and basic (□) solutions. Reproduced with permission.[19] Copyright 2010, American Chemical Society. (e) Tafel curves obtained from cyclic voltammetry measurement and chronoamperometry test in 0.1 M $HClO_4$ solution using $IrTiO_2$ as electrode. Reproduced with permission.[30] Copyright 2014, Royal Society of Chemistry.

Herein, we summarized the reported engineering strategies for TM-based water splitting electrocatalysts, including support effects, interface effects, crystal faces tuning, elemental doping, defects tuning, and some other strategies. To validate the versatility of each mentioned strategy, various common electrocatalysts for HER (TM-based carbides, alloys, sulfides, and nitrides) and OER (TM-based oxide, selenides, and phosphides) were referred to as examples for discussion. Moreover, how each strategy tunes the electrocatalysts to enhance the catalytic performances is also carefully illustrated in the following sections. This research review aims to: i) improve the conductivity and boost the electron transfer from catalysts to reactant species; ii) increase the active sites and engineer the active centers of TM-based catalysts to enhance the intrinsic activities; iii) tune the electronic structures of TM-based catalysts and optimize the adsorption abilities of intermediate species via feasible strategies to lower reaction barriers. By presenting reported results, current challenges, and opportunities, we hope that our work could be of assistance in designing and engineering cost-effective TM-based electrocatalysts for water splitting.

2. Electrochemistry of water splitting

2.1. Hydrogen evolution reaction

In general, a water splitting electrolyzer is consisted by cathod, membrane, anode and electrolyte, in which hydrogen evolution catalysts are coated on the cathode, and

H_2O are decomposed into H_2 at the surface of catalysts under a certain voltage. According to different electrolytes in which water splitting occurs, H_2 can be produced via different steps.

Acidic electrolyte:

$$2H^+ + 2e^- \rightarrow H_2$$

Neutral or alkaline electrolyte:

$$2H_2O + 2e^- \rightarrow H_2 + 2OH^-$$

HER involves three possible reaction steps. In acidic electrolyte, the first process is Volmer step ($H^+ + e^- \rightarrow H_{ads}$) to generate adsorbed hydrogen atom (H_{ads}) through the reaction of an electron with proton over the electrode surface. After the generation of H_{ads} species, H_2 production proceeds through the Tafel step ($H_{ads} + H_{ads} \rightarrow H_2$), the Heyrovsky step ($H_{ads} + H^+ + e^- \rightarrow H_2$), or both. In neutral or alkaline solution, the HER mechanism is still ambiguous, and the most accepted elementary reactions are Volmer step ($H_2O + e^- \rightarrow H_{ads} + OH^-$), Heyrovsky step ($H_{ads} + H_2O + e^- \rightarrow H_2 + OH^-$), and Tafel step. Hydrogen generation can proceed via Volmer–Heyrovsky, Volmer–Tafel, or Volmer–Heyrovsky/Tafel path. Regardless of the reaction routes, the H_{ads} species play an important role in HER, so its free energy (ΔG_{H^*}) could be an important descriptor for hydrogen-evolving catalysts. Optimal HER catalysts should possess a nearly zero ΔG_{H^*} to balance the adsorption and desorption of H and H_2. A volcano plot of different metal-based HER electrocatalyts (Figure 1c) has been summarized based on the exchange current density (j_0) and the M-H bond energies; this curve permits a comparison of catalytic performances and serves as a guide in developing highly effective metal-based electrocatalysts.[19] Therefore, volcano plots drawn based on reliable HER data of various electrocatalysts are valuable for researchers.

2.2. Oxygen evolution reaction

Oxygen evolution catalysts are utilized at the anode in water splitting electrolyzer, and oxygen gases are subsequently produced when an external potential is applied.

Nevertheless, the OER at anode is more complex than the HER because of its four-electron oxidation processes. The large overpotential of OER mainly restricts the development and application of water splitting. Hence, OER-related research has been intensively performed to develop optimal catalysts that can greatly minimize the overpotential of water electrolysis. Exploring the catalytic mechanism of OER is also important in designing advanced electrocatalysts. In general, the reaction mechanism changes when different pH electrolytes are employed (see below).

Acidic or neutral electrolyte:

$$2H_2O \rightarrow 4H^+ + 4e^- + O_2$$

Alkaline electrolyte:

$$4OH^- \rightarrow 2H_2O + 4e^- + O_2$$

Table 1. Possible elementary reaction steps of OER over oxides in both acid and alkaline aqueous solution.

Acid Solution	**Alkaline Solution**
(1) Electrochemical oxide path[20,21]	**(1) Electrochemical oxide path**[20,21]
$* + H_2O \rightarrow *–OH + H^+ + e^-$	$* + OH^- \rightarrow *–OH + e^-$
$*–OH \rightarrow *–O + H^+ + e^-$	$*–OH + OH^- \rightarrow *–O + H_2O + e^-$
$2*–O \rightarrow 2* + O_2$	$2*–O \rightarrow 2* + O_2$
(2) Oxide path[21]	**(2) Oxide path**[21]
$* + H_2O \rightarrow *–OH + H^+ + e^-$	$* + OH^- \rightarrow *–OH + e^-$
$2*–OH \rightarrow *–O + * + H_2O$	$2*–OH \rightarrow *–O + * + H_2O$
$2*–O \rightarrow 2* + O_2$	$2*–O \rightarrow 2* + O_2$
(3) Krasil'shchkov path[22]	**(3) Krasil'shchkov path**[22]
$* + H_2O \rightarrow *–OH + H^+ + e^-$	$* + OH^- \rightarrow *–OH + e^-$
$*–OH \rightarrow *–O^- + H^+$	$*–OH + OH^- \rightarrow *–O^- + H_2O$
$*–O^- \rightarrow *–O + e^-$	$*–O^- \rightarrow *–O + e^-$
$2*–O \rightarrow 2* + O_2$	$2*–O \rightarrow 2* + O_2$
(4) Wade and Hackerman's path[23]	**(4) Yeager's path**[24,25]
$2* + 2H_2O \rightarrow *O + *H_2O + 2H^+ + 2e^-$	$* + OH^- \rightarrow *–OH + e^-$
$*O + 2*OH^- \rightarrow 2* + *H_2O + O_2 + 2e^-$	$*^z–OH \rightarrow *^{z+1}–OH + e^-$
	$2*^{z+1}–OH + 2OH^- \rightarrow 2* + 2H_2O + O_2$

The possible elementary reaction steps of OER under alkaline or acidic solution conditions are summarized in Table 1, where M represents an active site on catalyst surfaces. In an acidic solution, the electrochemical oxide path has been the most accepted reaction mechanism, where H_2O adsorption and dissociation is the first and crucial step. Thus, regulating H_2O adsorption on electrocatalysts in acidic media can boost OER performances. Under alkaline condition, the OH^- adsorption on the active site is the first step, followed by different intermediate reaction steps. Among the elementary reaction steps of OER, the rate-determining step with highest reaction barrier could indicate the overpotential of the whole reaction. For ideal catalysts, the free energies of each elemental step should be similar and close to 1.23 V. Figure 1d exhibits the volcano plot of the OER overpotentials of TM oxide materials versus their transition enthalpy.[19] Obviously, RuO_2 and IrO_2 are positioned at the top due to intrinsic good conductivity as well as advisable electronic structures. Therefore, feasible engineering strategies can be developed for low-cost TM-based materials as promising candidates with noble metal catalyst-like properties for water splitting.

2.3. Evaluation of electrocatalysts

2.3.1. Overpotential (ŋ) and current density (j) at certain potentials

For both HER and OER, extra potentials larger than theoretical potential is required to trigger reactions, which is called as overpotential (ŋ).[26-28] The overpotential includes three categories, namely, activation, concentration, and that caused by the uncompensated resistance in the electrochemical interfaces for HER and OER. Activation overpotential has been the key parameter to evaluate catalysts, because it has the most important contribution to total overpotential. Concentration overpotential is generated from the sudden concentration drop of reactants and which could be minimized via stirring. While ohmic drop compensation can be used to optimize the resistance overpotential. The overpotential for HER and OER can be obtained from the

polarization curve tested by linear sweep voltammetry (LSV). Moreover, the current density (j) at high potentials based on LSV is another alternate activity parameter, especially for practical utilizations.

2.3.2. Tafel slope and exchange current density (j_0)

The Tafel plot can generally be derived from the LSV curve, where the slope values can be obtained using Tafel equation:[29]

$$\eta = a + b \log(j)$$

In this equation, b is the Tafel slope value, which suggests charge transfer abilities of an electrocatalyst. Therefore, the Tafel slope can describe the mechanism of electrode reactions. When η is set to 0, the obtained j is defined as exchange current density (j_0), which is often used to illustrate intrinsic activities of electrocatalysts. Owing to capacitive currents, scan rate greatly influences the LSV used for Tafel plot, thus possibly leading to errors in determining the Tafel slope and j_0 to some extent. Therefore, the steady state currents from i–t curves under various potentials should be used to accurately calculate the Tafel slope and j_0. A close comparison of Tafel slopes acquired by using j from CV and from chronoamperometric i-t curves for commercial $IrTiO_2$ catalyst is provided in Figure 1e.[30]

2.3.3. Long-term stability

The long-term stabilities of prepared materials are crucial indicators for their practical utilization and is usually evaluated by cyclic voltammetry (CV) accelerated degradation test at high scan rate, chronoamperometric, or chronopotentiometric approaches. The increase of onset potential or overpotential before and after CV tests indicates their stabilities. The smaller increase indicates a higher long-term stability. For chronoamperometry or chronopotentiometry testing, a fixed potential or current should be set to monitor the durabilities of catalysts.

2.3.4. Turnover frequency (TOF)

The TOF at certain overpotential is another instructive indicator for estimating the

catalytical activity of obtained electrocatalysts for HER and OER. TOF can generally be calculated by the number of moles of products generated per catalytic site per unit time. The TOF can exhibit the intrinsic activity of each catalytic site in the catalysts, but obtaining a precise TOF value is not easy due to difficulty in calculating the total catalytic sites of catalysts. A reasonable method to acquire TOF is to consider the surface atoms or the easily accessible atoms of the catalysts. The other TOF values are calculated by using an approach based on the total catalytic species in the catalysts.[31-34] TOF can provide useful insights on the comparative electrocatalytic performances of different catalysts when reasonable calculation is executed.

2.3.5. Faradaic efficiency (FE)

FE is a quantitative parameter applied to describe efficiencies of electron transfer from external circuit to desired products in the reaction system. For HER and OER, FE is defined as the ratio between quantity of H_2 or O_2 gas produced during the reaction and theoretical gas amount calculated from chronoamperometric or chronopotentiometric analysis.[35-37]

2.4. Design principles of electrocatalysts

HER and OER occur at the solid–liquid–gas interface with solid materials as electrocatalysts, liquid acid or alkaline aqueous solution as electrolytes, and H_2 or O_2 gas as the product. Primarily, the reactant (H^+, OH^-, or H_2O) is first adsorbed onto the catalyst surfaces. When a potential is applied, the electrons pass through catalysts to the interface, and an electrode reaction is then triggered to produce H_2 or O_2 gas. Finally, the gas products are released from the catalyst surface. Therefore, ideal catalysts should possess good chemical stability in acid or alkali electrolytes and under high potential conditions to achieve a good long-term working life. Given that HER and OER involve electron transfer through the catalysts, optimized catalysts should possess excellent electrical conductivity to facilitate electron transfer and effectively enhance the reaction rate. In addition, the proper abilities of reactant adsorption and product desorption are indispensable for good electrocatalysts. The binding abilities of multiple intermediates

of HER or OER over catalyst surfaces are also crucial, because when the binding energies are extremely high, the catalyst activity will be limited by the poisoning effect; however, when the species weakly bind to the active sites, activation over the electrocatalyst becomes difficult. Therefore, the proper binding energies of involved species are essential for the electrocatalysts and dramatically contribute to the catalytic performances. Moreover, low cost and environmental hazardless are also crucial requirements for objective electrocatalysts in large-scale water electrolysis.

Figure 2. Review scheme of design strategies, characterization, and theoretical analysis of high-performance TM-based electrocatalysts for large-scale water splitting application.

The above discussions have prompted the designing of advanced novel materials as catalysts or the engineering of traditional catalysts by facile strategies to obtain greatly enhanced performances. The following sections highlight the engineering strategies applied for traditional electrocatalysts to boost their HER or OER activities for pure H_2 production (as shown in Figure 2).

3. Engineering TM-based Electrocatalysts

3.1. Engineering by support effects

Coupling highly conductive supports with active nanomaterials has always been regarded as a promising approach to enhance the conductivity. At the same time, the electronic structures of active materials can also be engineered via support effects, further significantly affecting the electrocatalytic activities. As a result, the enhanced conductivity of as-prepared catalysts could contribute to fast charge transfer from catalysts to interfaces of catalysts and reactant, leading to fast reaction dynamics. Moreover, the tuned electronic properties of electrocatalysts can optimize the bonding capacities of intermediates over electrocatalysts during HER and OER, significantly reducing the reaction barriers. Therefore, various supports have been employed to enhance electrocatalytic performances of TM-based nanomaterials.[38-40] Particularly, carbon-based supports with high specific surface area and metal-based supports with good electrical conductivity were widely investigated in HER and OER.

3.1.1. Carbon-based support effects

Owing to good electrical conductivity, high specific surface area and easy modifiability, various carbon-based nanomaterials (such as graphene, heterogeneous atom doped porous carbon), have been employed to support active catalysts to boost their electron conductivity and tune the electronic structures, recently.[41-43] For instance, Lan's group synthesized a novel HER composite electrocatalyst containing molybdenum carbide and reduced graphene oxide (denoted as Mo_2C@NPC/NPRGO) through the pyrolysis of ternary polyoxometalate-polypyrrole/RGO precursor at 900 °C (Figure 3a).[44] The SEM and TEM images of as-obtained Mo_2C@NPC/NPRGO catalyst indicated that its morphology is similar to that of original precursors, and the Mo_2C possessing an average size of 2–5 nm was anchored on RGO surface at a high density. Clear lattice fringes of Mo_2C@NPC/NPRGO showed an interplanar distance of 0.238 nm in HRTEM image, suggesting the explored (111) planes of Mo_2C nanoparticles (NPs). In addition, the Mo_2C NPs are enveloped by carbon layers, preventing the aggregation of Mo_2C NPs as well as enhancing their stability during catalysis. As shown

in Figure 3b. the as-prepared Mo_2C@NPC/NPRGO electrocatalysts exhibited excellent HER activities with a low onset overpotential of 0 mV. Moreover, the overpotential to reach current density of 10 mA cm^{-2} (denoted as as η_{10}) of Mo_2C@NPC/NPRGO catalyst was low as 34 mV, much better than that of Mo_2C@NPC. The Tafel slope value of Mo_2C@NPC/NPRGO (Figure 3c) is approximately 33.6 mV/dec, which is superior to that of Mo_2C@NPC, confirming the roles of NPRGO support in boosting HER performances. Density functional theory (DFT) results in Figure 3d revealed that the Mo_2C@C-graphitic N possess the lowest ΔG_{H^*} value of 0.69 eV, verifying that the carbon support is important in tuning H bonding energy. Besides, Peng and co-workers synthesized Mo_2C/N-PC with nitrogen-doped porous carbon as the supporter. The prepared Mo_2C/N-PC catalyst showed excellent HER activities in 0–14 pH range. DFT calculations demonstrated that support effect can contribute to a decreased ΔG_{H^*}.[45] These experimental and theoretical results certified that the support effects of carbon-based materials could efficiently boost HER activities by engineering the conductivity and electronic structures of catalysts. In addition, alloy FeCo NPs completely encapsulated in carbon (with a thickness of approximately 1.71 nm) were successfully prepared via pyrolysis of metal–organic frameworks.[46] Due to the support effect, as-prepared catalyst exhibited enhanced catalytic HER activities. DFT calculations indicated that the electronic structures of composite catalysts was regulated through carbon layer support effect. Similarly, RuCo anchored on N-doped porous carbon nanomaterials were also synthesized via a method of annealing Prussian blue analogs under N_2 atmosphere as illustrated in Figure 3e.[47] These RuCo/NC catalysts consist of abundant alloy RuCo NPs (about 30 nm) coated with carbon (from 1 to 15 layers). Calculated charge-density difference of Co_3Ru model (Figure 3f) confirms that the transfer of electrons from metals to graphene supports is beneficial in lowering the ΔG_{H^*}. As HER catalysts, the RuCo/NC with Ru content of 3.58 wt.% (denoted as S-4) displayed a η_{10} of 28 mV (Figure 3g) in 1 M KOH aqueous media, which is superior to that of Pt/C. Furthermore, Tafel slope (Figure 3h) of S-4 sample is 31 mV dec^{-1}, closed to that of Pt/C, which suggests a rapid HER rate and Tafel–Volmer mechanism for this

RuCo/NC catalyst. DFT calculations (Figure 3i) illustrated that the ΔG_{H^*} could be reduced by the combination of metal NPs and graphene. The Ru_3Co-N-doped graphene structure has a optimal ΔG_{H^*} value (0.31 eV), thus confirming the roles of carbon-based support in improving HER performances.

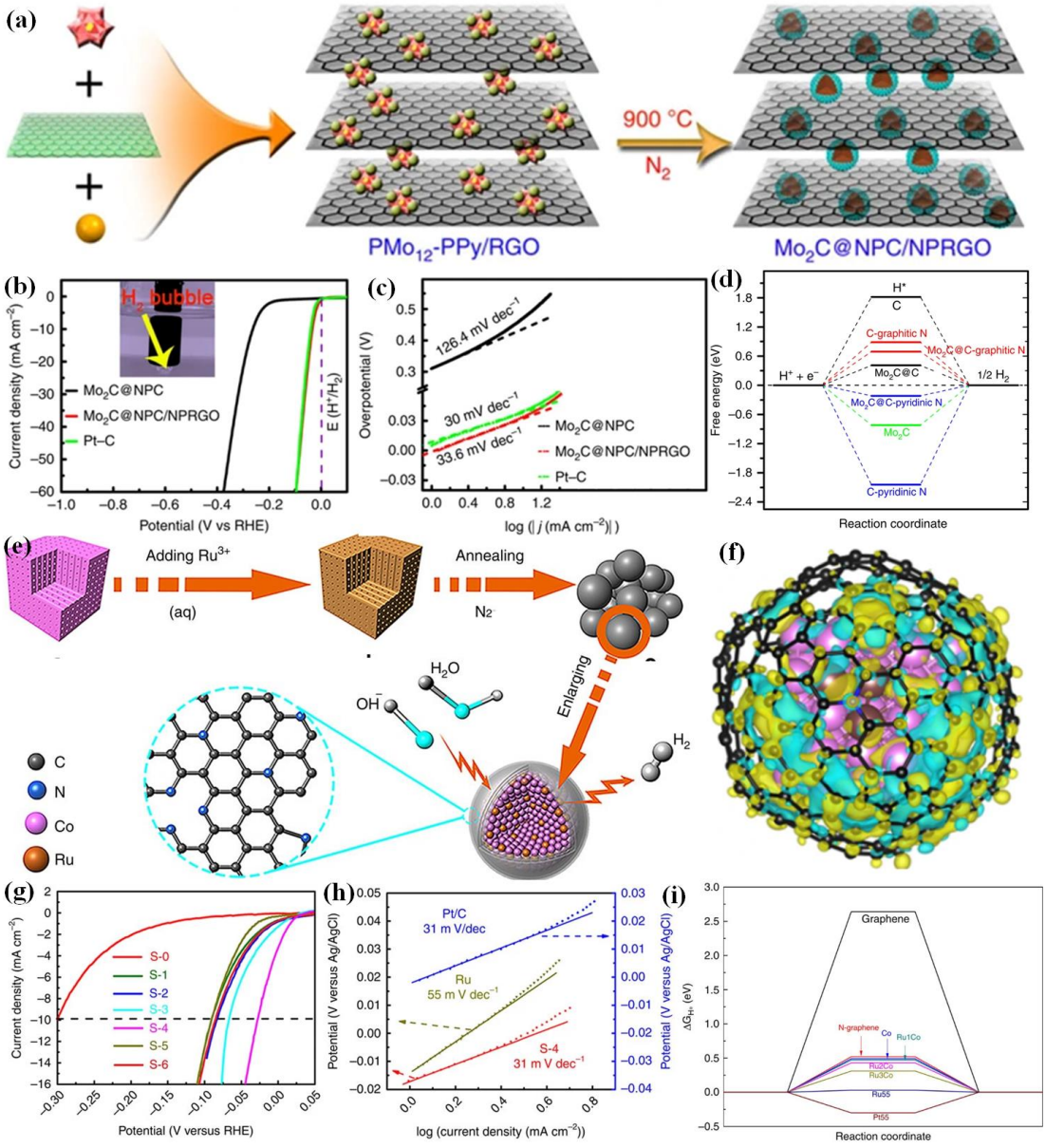

Figure 3. (a) Schematic illustration for synthesizing Mo_2C@NPC/NPRGO composite catalyst. (b) The LSV curves for HER and (c) Tafel plots of catalysts in 0.5 M H_2SO_4 electrolyte. Inset in (b): H_2 bubbles produced over the Mo_2C@NPC/NPRGO catalyst. (d) The ΔG_{H^*} of related catalysts. Reproduced with permission.[44] Copyright 2016, Nature Publishing Group. (e) The synthetic process of RuCo@NC as HER

electrocatalysts. (f) Calculated charge-density differences of Co_3Ru with color region isosurface value of 0.01 e $Å^{-3}$. (g) LSV curves for HER of RuCo@NC samples in 1 MKOH solution. (h) Tafel slope plots of Pt/C, Ru and S-4 catalysts. (i) Calculated ΔG_{H^*} over different electrocatalysts. Reproduced with permission.[47] Copyright 2017, Nature Publishing Group.

OER is more kinetically sluggish than HER due to its multistep oxidation, and support effects can also work as a potential method to enhance OER performances by engineering conductivities and electronic structures of TM electrocatalysts. For example, Yu and co-workers reported NG-$CoSe_2$ catalyst contianing $CoSe_2$ nanobelts and N-doped graphene oxides for OER in 0.1 M KOH solution.[48] Graphene possessing good electrical conductivity was selected as support to anchor $CoSe_2$ nanobelts. After hydrothermal reaction as shown in Figure 4a, flexible $CoSe_2$ nanobelts were tightly loaded on the NG surfaces. TEM image clearly illustrated that the ultra-long belt-like $CoSe_2$ was anchored on NG sheets, and the obtained nanobelts consisted of numerous $CoSe_2$ NPs. Moreover, the (211) plane of cubic $CoSe_2$ and graphene (001) plane were clearly observed in the catalyst. The as-prepared NG-$CoSe_2$ as OER electrocatalysts displayed smaller onset overpotential (0.293 V) and higher catalytic current than $CoSe_2$ nanobelt references (Figure 4b), as well as lower Tafel slope 40 mV/dec. These enhanced OER activities mainly originated from the support effects involving intimate connections between $CoSe_2$ and NG (Figure 4c and 4d). Li and co-workers reported $CoSe_2$ nanowires combined with nitrogen-doped carbon ($CoSe_2$@N-CNWs), which could act as a potential OER catalyst in 1.0 M KOH media. Due to the enhancement of electric conductivity, optimized free adsorption energy of OER intermediates, these $CoSe_2$@N-C NWs exhibited an enhanced 6.61-fold catalytic activity than $CoSe_2$ NWs at η of 340 mV.[49] Additionally, $Co_3(PO_4)_2$ NPs coated by N-C were prepared by using bifunctional O-phospho-DL-serine reagent.[50] SEM and TEM images clearly showed the $Co_3(PO_4)_2$ NPs are approximately 100 nm. HRTEM revealed that $Co_3(PO_4)_2$ NPs were supported by N-doped carbon layers. In 1 M KOH media, the obtained $Co_3(PO_4)_2$@N-C exhibited excellent performances toward OER with a amall η_{10} of 317

mV and a low Tafel slope value of 62 mV dec^{-1}, which are superior to that of pure $Co_3(PO_4)_2$ catalyst. The excellent activities are benefitted from the abundant active sites of $Co_3(PO_4)_2$ NPs and high electrical conductivity caused by N doped carbon layers. FeOOH is also regarded as a promising catalyst for OER, but its intrinsic poor electron conductivity hinders catalyzing OER. Li's group presented depositing FeOOH particles onto ZIF-derived N-doped carbons (NPCs) as shown in Figure 4e could improve the electron conductivity and boost the catalytic performances.[51] In alkaline media, this FeOOH/NPC catalyst exhibited a small η_{100} of 230 mV (Figure 4f) and a low Tafel slope of 33.8 mV dec^{-1} (Figure 4g), as well as good durability (Figure 4h). Besides, many TM-based electrocatalysts supported by carbon-based matrix have been reported, confirming that carbon-based support effects could efficiently enhance the catalytic activities via improving the conductivity and tuning the electronic structures.[52-60]

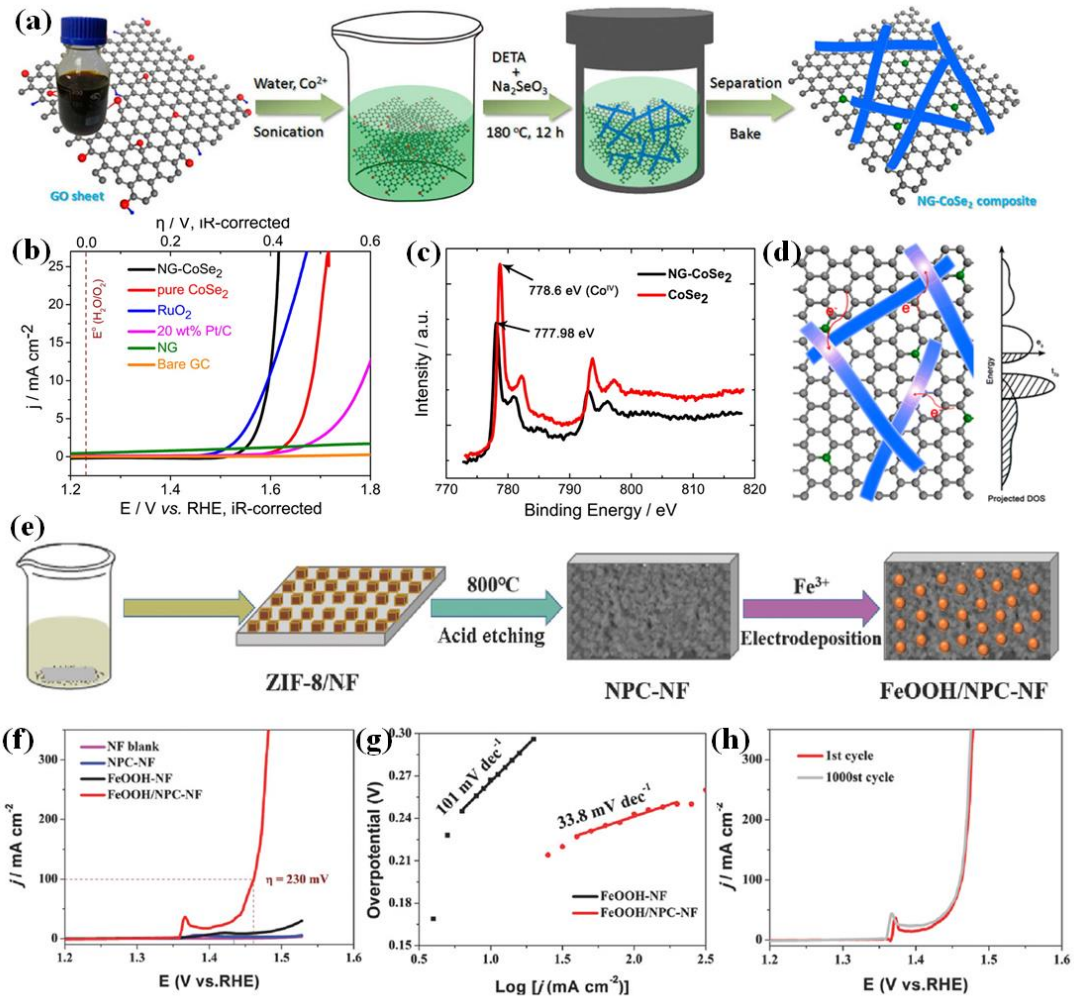

Figure 4. (a) Schematic illustration for constructing NG-$CoSe_2$ composite electrocatalyst. (b) The LSV curves towards OER of catalysts. (c) High-resolution XPS spectra of Co 2p. (d) The electron donation image of NG-$CoSe_2$ and the schematic DOS of $CoSe_2$. Reproduced with permission.[48] Copyright 2014, American Chemical Society. (e) The fabrication process of FeOOH/NPC-NF electrode. (f) The LSV curves for OER, and (g) related Tafel plots. (h) LSV curves for stability assessment. Reproduced with permission.[51] Copyright 2018, Wiley-VCH.

3.1.2. Metal-based support effects

Metal-based supports possessing richer electrons and better conductivity than carbon have been widely employed as promising supports and mediators to engineer the activities of electrocatalysts. In 2014, Jen's group utilized periodic DFT with BEEF-vdW functional to explore HER performances on supported MoS_2 catalysts, including MoS_2, MoS_2-Au, and MoS_2-graphene three different systems.[61] Compared to MoS_2, the ΔG_{H^*} values of MoS_2-Au and MoS_2-graphene have been increased by 0.56 and 0.18 eV. This work also revealed that support effects could greatly change the H binding energy, which contributes to several orders of magnitude improvement. In 2017, experimental results further confirmed the role of metal support effects on boosting electrocatalytic HER activities.[62] $[Mo_3S_{13}]^{2-}$ cluster anchored on Au, Ag, Cu, and GC supports were prepared, and $[Mo_3S_{13}]^{2-}$ on Au support showed the smallest onset potential that was better than $[Mo_3S_{13}]^{2-}$ on glassy carbon. Related DFT calculation proved that metal Au support can efficiently tune the ΔG_{H^*} of electrocatalysts for HER. For OER electrocatalysts, metal-based supports are usually employed to boost the catalytic performances by regulating electronic properties and improving conductivity. For instance, cobalt oxide films with a thickness of 0.4 monolayer were deposited onto various metal supports.[63] In 0.1 M KOH solution, cobalt oxide/Au sample displayed the most remarkable enhancement of anodic currents (Figure 5a), revealing that Au

support surely improves catalytic performances of cobalt oxide catalysts. Calulated TOF of cobalt oxide films on different metal supports showed that cobalt oxide/Au sample was 40 times better than pure cobalt oxide. Moreover, the catalytic OER performances of cobalt oxide supported by different metals increased with increasing electronegativity of metals (Co < Cu < Pd < Pt < Au). Experimental and theoretical results revealed that the increase in Co^{IV} cations in the supported cobalt oxides caused by metal-substrate is greatly attributed to these enhanced OER activities. In 2017, a self-supporting electrode consisted of Co_2P NPs anchored on Co foil was synthesized via the one-step phosphorization method (Figure. 5b).[64] The SEM image in Figure 5c shows that the Co_2P NPs were uniformly fixed on the surface of Co foil after phosphorization, thereby generating a continuous and porous film on the Co foil surfaces, which could greatly enlarge contact area of Co_2P NPs and electrolyte. The TEM image in Figure 5d of Co_2P displayed an irregular NP morphology, and the HRTEM image (Figure 5e) exhibited the clear lattice spacing of 0.22 nm, confirming the exposed (112) crystal plane of Co_2P. Figure 5f and 5g show the HER and OER performances of Co_2P/Co-foil electrode and the Co_2P NPs peeled off from the integrated electrode. In 1 M KOH solution, the Co_2P/Co-foil integrated electrode showed superior activites with η_{10} of 157 mV for HER and 319 mV for OER, respectively, which are better than those of pure Co_2P NPs. Finally, this integrated Co_2P/Co-foil can work as bifunctional electrodes and exhibits excellent overall water splitting activities (Figure 5h). These results confirmed that the metal-based support effects hugely contribute to conductivities and electrocatalytic activities. Results mentioned above reveal that support effects could tremendously enhance the conductivity and significantly tune electronic structures of active materials, leading to optimized adsorption abilities, as well as reduced reaction barriers, further greatly boosting the electrocatalytic activities. Accordingly, engineering the electronic structures of TM-based active materials using support effects in electrocatalysts could be an effective method for boosting electrocatalytic water splitting.[65-70]

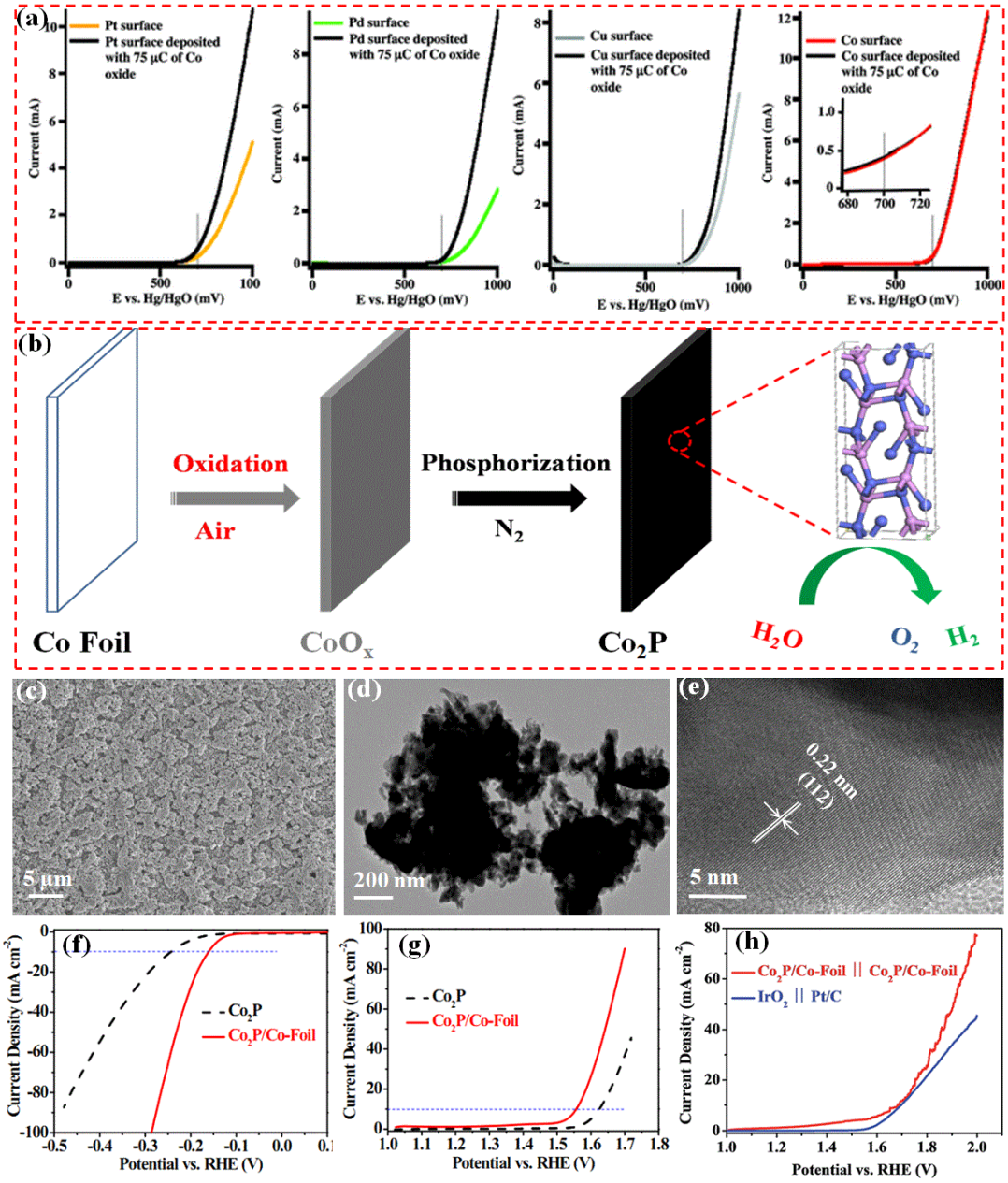

Figure 5. (a) The LSV curves of various metal electrodes with/without Co oxide in 0.1 M KOH, and dotted line marks 700 mV. Reproduced with permission.[63] Copyright 2011, American Chemical Society. (b) Schematic illustration for preparing Co_2P/Co-foil self-supporting bifunctional electrode. (c) The SEM, (d) TEM and (e) HRTEM images of Co_2P NPs. LSV curves for HER (f) and OER (g) of Co_2P particles and the integrated Co_2P/Co-Foil electrode. (h) LSV curves of Co_2P/Co-foil||Co_2P/Co-foil and IrO_2||Pt/C for water electrolysis in 1 M KOH solution. Reproduced with permission.[64] Copyright 2017, Royal Society of Chemistry.

3.2. Engineering by interface effects

Different from support effects, the interface effects generally equip the hybrid electrocatalysts with more active sites at the interfaces. Besides, the strong electronic interaction of different active materials can lead to higher combined catalytic performances than individual components.[71,72] Moreover, abundant interfaces in the hybrid electrocatalysts bring diverse engineered electronic features that are favorable for optimizing theie chemisorption abilities and further enhance their HER or OER kinetics.[73,74] Therefore, engineering the catalysts using the strategy of interface effects is essential to boost catalytic activities and accelerate reaction kinetics via increasing the active sites and tuning electronic structures. For instance, Markovic's group prepared a $Ni(OH)_2$/Pt composite material that can be used as a HER electrocatalyst, which contains uniform $Ni(OH)_2$ clusters with height of 0.7 nm and size of 8–10 nm.[75] CV curves revealed that the $Ni(OH)_2$/Pt electrocatalyst displays better adsorption and irreversible reduction of OH_{ad} compared with pure Pt electrode because of the high oxophilicity of $Ni(OH)_2$ clusters. Consequently, the $Ni(OH)_2$/Pt hybrid material exhibited an eightfold increase in HER activity in 0.1 M KOH solution compared with Pt material, suggesting that the interface effects improves the catalytic HER performances. DFT calculations revealed that the forceful interaction of $Ni(OH)_2$ with O atoms and Pt with H atoms can synergistically enhanced the H_2O adsorption on the interfaces of $Ni(OH)_2$/Pt electrocatalyst. Moreover, the edges of $Ni(OH)_2$ clusters at the interfaces boost the dissociation of water and production of H intermediates, and H is then easily adsorbed on Pt surfaces.

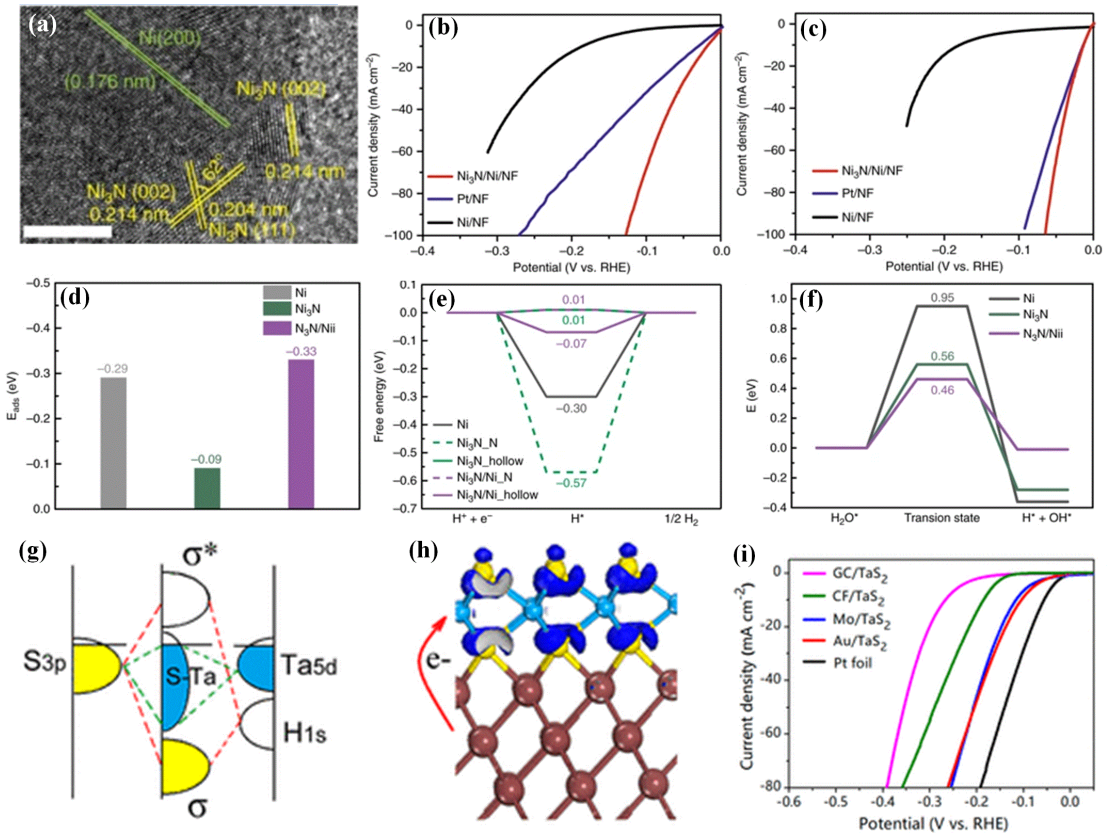

Figure 6. (a) The HRTEM image of Ni_3N/Ni catalyst, scale bar: 5 nm. The corresponding LSV curves for HER in 1.0 M potassium phosphate (KPi) buffer (b) and 1.0 M KOH electrolyte (c). (d) Adsorption energy of H_2O molecule over different sites. (e) The ΔG_{H^*} and (f) reaction barrier of H_2O dissociation over Ni, Ni_3N, and Ni_3N/Ni. Reproduced with permission.[76] Copyright 2018, Nature Publishing Group. (g) Schematic diagram of molecular orbitals for H-TaS_2. (h) Charge density distribution of Au/TaS_2, where Au, Ta, S, and H are shown as brown, blue, yellow, and white spheres, respectively. (i) The electrocatalytic HER performance of TaS_2 samples on different substrates. Reproduced with permission.[77] Copyright 2019, American Chemical Society.

Sun et al. reported that interfacing Ni_3N and Ni is a promising method of increasing active sites and engineering electronic structures for highly active HER in aqueous media, in which Ni_3N/N was synthesized through cathodic electrodeposition, followed by facile thermal nitridation.[76] Figure 6a shows the HRTEM image of as-prepared Ni_3N/Ni sample with interfaces of hexagonal Ni_3N and Ni metal. Lattice fringes clearly indicated the exposed faces of the Ni_3N/Ni sample are (111) and (002) planes of Ni_3N,

and the (200) plane of cubic Ni. Figure 6b and 6c displayed electrocatalytic HER performances of Ni_3N/Ni on Ni foams in H_2-saturated electrolytes, where the Ni_3N/Ni/NF electrode showed remarkable η_{10} of 19 and 12 mV in 1.0 M KPi buffer and 1.0 M KOH, respectively. However, the Ni/NF electrode and Pt/NF displayed mediocre HER performances, suggesting the critical role of the interfaces between Ni_3N and Ni. DFT was conducted to further investigate the role of interfaces in improving catalytic activities. The ΔG_{H^*} values at two positions of Ni_3N/Ni_N and Ni_3N/Ni_hollow (Figure 6d) are 0.01 and - 0.07 eV, which are smaller than those of pure Ni (- 0.3 eV) and pure Ni_3N site (- 0.57 eV). This finding confirms that the interface effects could reduce H binding affinity on the Ni_3N/Ni surface. Figure 6e displays the adsorption and dissociation of H_2O over electrocatalyst surfaces, that are paramount steps of HER in neutral and alkaline conditions. The adsorption energies along with the optimized structures suggest that the H_2O molecules tend to reside along the interfaces, which could greatly facilitate the subsequent H_2O dissociation on Ni_3N/Ni. The diagrams of the H_2O dissociation barrier (Figure 6f) show that Ni_3N/Ni holds the lowest energy barrier of 0.50 eV, smaller than those of Ni_3N and Ni. These DFT results proved that interface effects could engineer the electronic structures to further optimize the H and H_2O binding affinities, reduce the reaction barriers, and facilitate water dissociation. Liu and co-worker proposed that the HER performances of metallic 2D TaS_2 can be tuned via lattice mismatch and electron injection between electrocatalysts and the underlying substrates caused by interfacial engineering.[77] A series of 2D TaS_2 was successfully grown on different substrates via two-zone chemical vapor deposition. The schematic of molecular orbitals for H-TaS_2 (Figure 6g) shows that Ta and H atoms donate electrons to S. The charge density distribution (Figure 6h) displays that electrons are injected TaS_2 from the metallic substrates, which could weaken S−H and S−Ta bonds and lead to smaller ΔG_{H^*}. Consequently, TaS_2 on Au foil offered the best enhanced performances with lowest overpotential and smallest charge transfer resistance in the catalytic LSV curves (Figure 6i), revealing the validity of interface effects for engineering catalysts. He and co-workers fabricated a Ravenala leaf-like

$W_xC@WS_2$ heterostructure on carbon fibers (CFs) through carbonizing WS_2 nanotubes (NTs).[78] During synthesis, the outer walls of the WS_2 NTs were partially unzipped and had the appearance of nanoscale W_xC, which was attached to the inner tubes. LSV curves with iR-correction in Figure 7a displays that this $W_xC@WS_2$ catalysts required a low η_{10} of 146 mV, which is 172.7 and 46 mV smaller than those of pure WS_2 and W_xC at the same conditions, respectively, suggesting the crucial roles of interface effects. Figure 7b shows that the related Tafel slope of $W_xC@WS_2$-20 was 61 mV dec^{-1}, indicating a two-electron-transfer process with Volmer–Heyrovsky mechanism. This value is also smaller than those of pure WS_2 (110 mV dec^{-1}) and W_xC (68 mV dec^{-1}). DFT calculations revealed that interface effects could induce charge redistribution in heterostructures and optimize the adsorption and desorption abilities of catalysts to boost their HER performances. Free energy diagram showed that the ΔG_{H^*} over pure W_2S is approximately 2.26 eV, suggesting that the W_2C tightly binds H atoms and further hinders the H_2 desorption on its surface. When interfacing W_2C with WS_2, an electron transfer of 0.12 e from W_2C to WS_2 was detected in the charge redistribution in $W_2C@WS_2$ heterostructure (Figure 7c and 7d), which strongly implied the decrease of its ability of binding H atoms. In 2019, the engineered W_2N/WC heterostructures with abundant interfaces were prepared via a facile solid-state synthesis method.[79] During this process, volatile CN_x species generated from dicyanodiamide at high temperature could be trapped by WO_3 nanorods, and then the heterostructure catalysts were produced. Interestingly, the components in samples can be regulated by altering the synthesis temperature. When pyrolysis temperatures of 600 ºC, 700 ºC and 800 ºC were applied, the WO_3/W_2N heterostructures, pure W_2N and W_2N/WC heterostructures were obtained, respectively. The corresponding models and HRTEM images of WO_3/W_2N, pure W_2N and W_2N/WC heterostructures were shown in Figure 7e-7j. From HRTEM image of W_2N/WC sample, the lattices with 0.238 nm for W_2N (111) plane and 0.252 nm for WC (100) plane were clearly observed, confirming the abundant interfaces between W_2N and WC. The XPS spectra showed that the binding energy of W 4f in W_2N/WC was higher (1.0 eV) than that in pure W_2N, stating the extra charges

in the W 4f side and charge accumulation in W_2N due to these existing interfaces. As OER electrocatalysts, the W_2N/WC heterostructures displayed excellent performances with a low η_{10} of 320 mV, superior to that of the W_2N and WC catalysts (Figure 7k). The Tafel slopes plots showed that the W_2N/WC heterostructures possessed smaller value of approximately 94.5 mV dec^{-1} than other samples, and the TOF value of W_2N/WC heterostructures was 0.15 s^{-1} at 1.60 V, which is also higher than WO_3/W_2N (0.1 s^{-1}), and W_2N (0.03 s^{-1}). For HER, the W_2N/WC electrocatalyst exhibited a small η_{10} of 148.5 mV and a low Tafel slope value of 47.4 mV dec^{-1} (Figure 7l). DFT and XANFS analysis revealed that interfaces in W_2N/WC synergistically facilitated charge transfer, tremendously enhancing the electrocatalytic performances. Inspired by these results, many hybrid electrocatalysts with abundant interfaces have been reported, where more active sites were created, and the electronic structures were regulated for greatly boosting the electrocatalytic performances.[80-88] However, the fundamental mechanisms and structure-activity relationships of interface effects between active components still remain elusive because of their complexity.

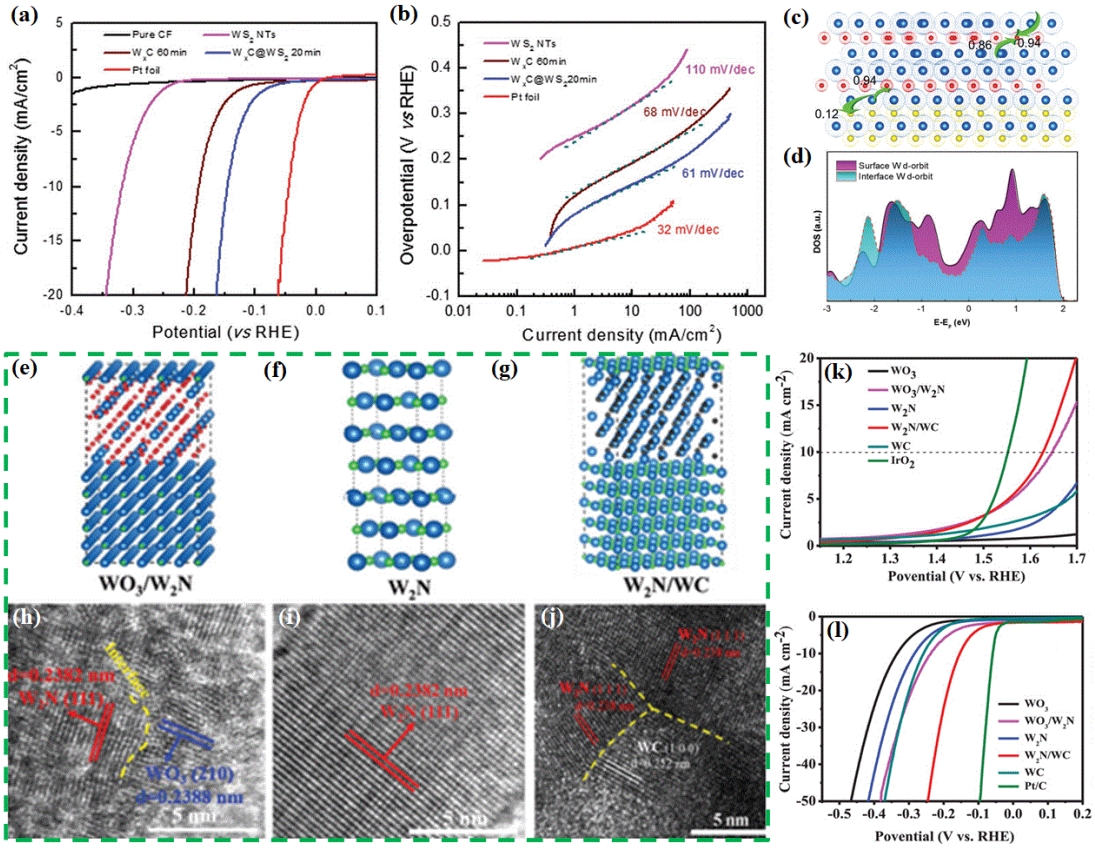

Figure 7. (a) The HER LSV curves and (b) Tafel slope plots for obtained $W_xC@WS_2$-20 and reference samples. (c) Calculated charge redistribution in $W_2C@WS_2$ heterostructure and (d) DOS comparison of the W located at different position. Reproduced with permission.[78] Copyright 2017, Wiley-VCH. (e-g) The representative models and (h-j) their corresponding HRTEM images of obtained WO_3/W_2N, W_2N, and W_2N/WC, respectively. (k) Experimental OER LSV curves, and (l) HER LSV curves of WO_3/W_2N, W_2N, W_2N/WC, and WC heterostructure electrocatalysts and noble metal catalysts. Reproduced with permission.[79] Copyright 2017, Wiley-VCH.

3.3. Engineering by crystal face

Principally, the catalytic activities of electrocatalysts for a specific reaction are highly dependent on the arrangement of atoms on the exposed surfaces, determining their adsorption and desorption abilities, and the amount of active centers. Therefore, regulating the type of the exposed crystallographic plane could greatly improve the performances of electrocatalysts for various reactions. Efforts have been devoted to studying the relationships between faceting and catalytic performances during the past several decades.[89-91] The high-index faceted nanocrystals generally possess higher energy surfaces, which could increase specific activity, while the low-index faceted materials with lower energy surfaces could provide good catalytic stability.[92-94] For HER electrocatalysis, the previous works approximately the dependence of HER activities vs. Pt catalyst facets have uncovered that the activities decreased with the decrasing activation energis of (110) > (100) > (111).[95,96] Furthermore, Markovic and co-workers in 2014 reported a study on the functional law between the activity and stability for OER of Ru single-crystal catalysts.[97] Consequently, the OER stabilities of Ru crystals increase in the order (001) > (110) > (111). The (001) face with Ru atoms possessing the highest coordination numbers and the lowest surface energies, is the most stable morphologically, which could reduce the generation and dissolution of higher state Ru species. These findings inspire us to regulate the exposed crystal plane surfaces where the electrochemical reactions occur to boost the electrocatalytic

performances of TM-based nanocatalysts.[98-101] For instance, Ma and his co-workers synthesized surface-tailored Co_3O_4 supported on N-doped reduced graphene oxide (N-rGO) to regulate the active sites of Co_3O_4 spinel for OER.[102] As shown in Figure 8a, three Co_3O_4 nanocrystals with different shapes and terminal faces anchored on N-rGO were prepared through a hydrothermal method. The morphologies of objective Co_3O_4 nanostructures on 2D N-rGO were easily tuned from nanocube (Nc) to nanooctahedron (NTO) and then nanopolyhedron (NP) using this synthesis process by simply changing the dosage of $Co(NO_3)_2$, $NH_3 \cdot H_2O$ and corresponding GO solution. These as-prepared Co_3O_4-NC/N-rGO, Co_3O_4-NTO/N-rGO and Co_3O_4-NP/N-rGO were terminated with {001}, {001} + {111}, and {112} planes, respectively, which were featured by different concentrations and distributions of Co^{2+}/Co^{3+} active sites on these exposed surfaces. The surface atomic arrangements in the {001}, {111} and {112} planes in the Co_3O_4 are displayed in Figure 8b–d, where the {001} or {111} planes only possess tetrahedrally coordinated Co^{2+} (Co^{2+}_{Td}) sites under normal condition, while the {112} plane not only has Co^{2+}_{Td}, but also possesses octahedrally coordinated Co^{3+} (Co^{3+}_{Oh}) sites. In theory, the Co^{3+}_{Oh} sites could act as superior active sites to Co^{2+}_{Td} species in efficient adsorption, activation and desorption processes, suggesting that the {112} faceted Co_3O_4-NP/N-rGO with abundant Co^{2+}_{Td} and Co^{3+}_{Oh} sites is more active than Co_3O_4-NTO/N-rGO and Co_3O_4-NC/N-rGO for OER. Electrochemical results in Figure 8e exhibits that Co_3O_4-NP/N-rGO terminated by the unusual {112} crystal plane owns superior OER performances than that of Co_3O_4-NC/N-rGO and Co_3O_4-NTO/N-rGO. Ho and co-workers successfully prepared high-index {112} faceted and defective Co_3O_4 nanosheets via a facile hydrothermal and $NaBH_4$ reduction strategy.[103] Remarkably, the obtained porous Co_3O_4 nanosheets with exposed {112} faces exhibited better activities toward OER with a lower η_{10} of 318 mV than those of {110} or {111} faceted porous Co_3O_4 nanosheets. The exposed {112} high-index facets with higher ratio of Co^{2+}/Co^{3+} contributed to accelerating charge transfer and increasing active sites. In addition, Ni_3S_2/NF electrode consisted of high-index faceted Ni_3S_2 nanosheets on nickel foam was synthesized by Zou et. al. by a in situ synthetic method.[104] As binder-

free electrodes, the obtained Ni_3S_2/NF materials showed highly active bifunctional performances towards both HER and OER. As depicted in Figure 8f and 8g, the high-index faceted Ni_3S_2/NF electrode needs small η_{10} of 223 and 260 mV for HER and OER in basic electrolyte, respectively. Moreover, the self-supported Ni_3S_2/NF electrode showed approximate 100% FE and remarkable durability (> 200 h) for both HER and OER. The activities for HER of the different faced surfaces were explored using DFT computations (Figure 8h-j). Three different kinds of S-sites on Ni_3S_2 (210) surface were simulated and the calculated ΔG_{H^*} values were 0.623 eV, 0.520 eV and 1.018 eV, which are smaller than that on the (001) surface, confirming the HER activity is higher on (210) surface. The S-sites with lower coordination number located at the deges of (210) surface mainly contribute to the excellent oerformances. Mu's group revealed that the exposed (222) plane in tantalum carbide (TaC) electrocatalysts could be more effective than other facets toward catalyzing HER by using theoretical calculations, and subsequently a new "micro-cutting-fragmentation" method was presented to synthesize the TaC with abundant high-index (222) exposed facets.[105] Calculated band structure in Figure 8k shows that no band gap is detected for all facets of TaC, implying its high conductivity, which is quite important for electrocatalytic HER. As shown in Figure 8l, the high-index TaC (222) facet displays a smaller ΔG_{H^*} value (− 0.23 eV) than (311), (220), (200) and (111) facets, further suggesting its best electrocatalytic activity over (222) facet. The as-prepared TaC NCs@C catalysts display a low onset potential (Figure 8m), a small Tafel slope (Figure 8n), and excellent stability for HER.

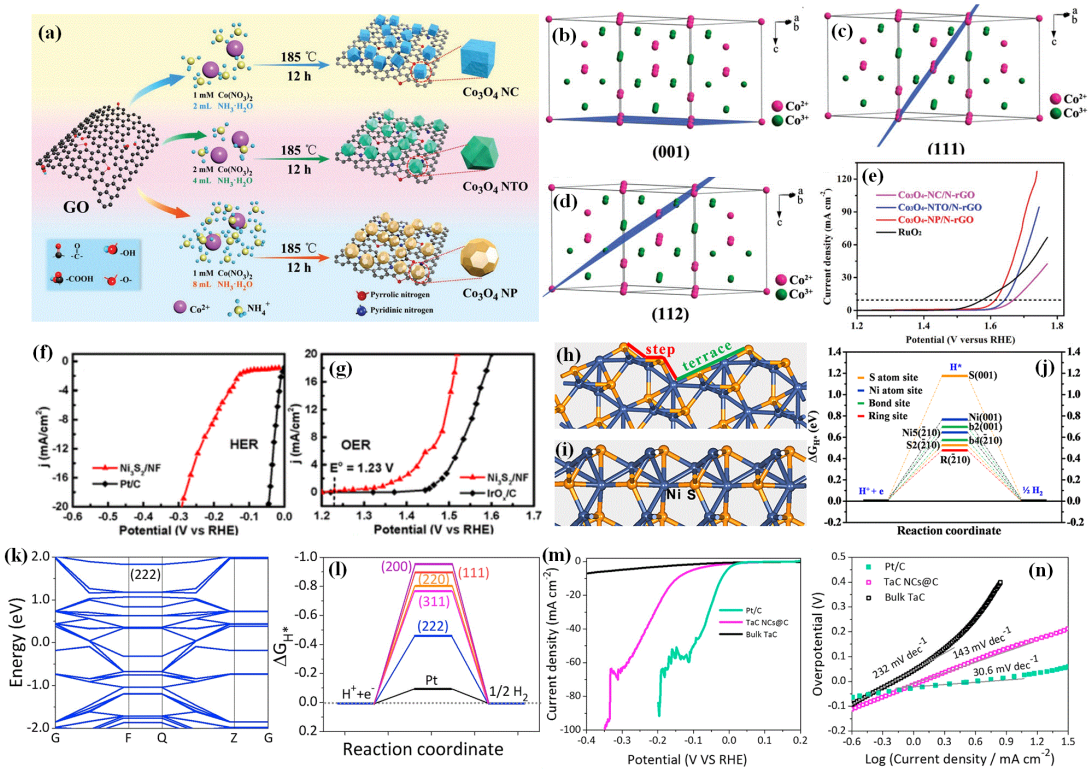

Figure 8. (a) Schematic illustration of synthesizing Co_3O_4 nanocrystals with different . (b-d) The Co^{2+}/Co^{3+} surface atomic configurations on (001), (111) and (112) planes in Co_3O_4. (e) LSV curves towards OER in 1 M KOH aqueous solution. Reproduced with permission.[102] Copyright 2017, Wiley-VCH. Steady-state current densities vs. applied potentials over high-index faceted Ni_3S_2 nanosheet arrays for HER (f) and OER (g). The most optimal terminations of (210) (h) and (001) (i) surfaces of Ni_3S_2. (j) The ΔG_{H^*} diagram of HER calculated over (210) and (001) surfaces of Ni_3S_2. Reproduced with permission.[104] Copyright 2015, American Chemical Society. (k) Band structure of high-index TaC (222) facets obtained by DFT. (l) Calculated ΔG_{H^*} diagram of HER for high-index (222) facet, relatively low-index (111), (200), (220) and (311) facets of TaC as well as Pt reference. (m) and (n) The LSV curves and corresponding Tafel plots in 0.5 M H_2SO_4 solution. Reproduced with permission.[105] Copyright 2017, Elsevier Inc.

In conclusion, tuning the density of highly exposed catalytically favorable faces in various nanomaterials is a promising strategy to reconstruct active sites in the catalysts, and optimize their related adsorption and desorption energies to boost the electrocatalytic performances. Numerous efforts have been made to develop facile

strategy for tuning the exposed faces,[106-112] however, due to the different surface energies of exposed faces, stable and catalytically favorable pure faces always evolve or disappear during their synthesis or application process. Therefore, engineering the nanocatalysts with favorable exposed faces to significantly improve their catalytic performances toward is still a challenge yet.

3.4. Engineering by elemental doping

Introducing other metal or nonmetal elements with different electron configurations into the lattice of TM-based electrocatalysts can lead to subtle distortion of the atomic arrangement, further regulate the active centers, and increase the active sites, change the electronic structures, and markedly tune the adsorption abilities of the catalyst surfaces. Therefore, engineering the catalysts by elemental doping has been a potential method to boost their water splitting performances.[113-116] For instance, Wu's group in 2010 synthesized Ni-doped Co_3O_4 nanowire arrays anchored onto a Ti foil. Results revealed that Ni dopants could lead to enhanced electronic conductivities and more active sites of the Co_3O_4, further improving OER performances.[117] Zhang and co-workers proposed an N-doped CoP electrocatalyst, and the LSV curves (Figure 9a) displays that the N-doped CoP sample on CC requires a small η_{10} of 42 mV; this is better than pure CoP, indicating that N doping could greatly boost the HER activities of CoP.[118] The effect of N doping on HER performances was explored by DFT calculations. As depicted in Figure 9b, the CoP (101) surfaces possessed a ΔG_{H^*} value of − 0.52 eV, suggesting a strong adsorption of H. While after N doping, the related ΔG_{H^*} value increased to − 0.14 eV, which is more thermo-neutral than that of pure CoP. Moreover, the calculated DOS of CoP and N doped CoP in Figure 9c illustrated that N doping could lead to downshift of d-band and weaken the H adsorption on their surface because N has stronger electronegativity than phosphorus. Yan and his co-workers revealed that elemental doping could efficiently modulate the electrocatalytically active center of Cu_7S_4 for OER.[119] As shown in the LSV curves (Figure 9d), the Co-Cu_7S_4 with the

atomic ratio of Co/(Co+Cu) of 0.07 (denoted as Co-Cu_7S_4-0.07) exhibited the best OER activity with a small η_{10} of 270 mV, superior to bare Cu_7S_4 and commercial IrO_2. Figure 9e displays the profiles of the free energy changes of OER over Cu_7S_4 and Co doped Cu_7S_4, and Figure 9f shows the feasible OER mechanism for the Co engineered Cu_7S_4 catalyst. These results stated the Co doped Cu_7S_4 with modified electronic structure could accelerate electron transfer between the active sites, increase the active sites, and lower the energy barriers. Similarly, Zhao and his co-workers reported that cobalt covalent doping could bring enhanced HER and OER bifunctionalities to MoS_2.[120] The HER LSV curves in Figure 9g exhibit that Co-MoS_2 with Mo/Co molar ratio of 21 (denoted as Co-MoS_2/BCCF-21) displayed superior HER performances with a low onset potential of − 0.02 V, which is better than that of MoS_2/BCCF. The OER LSV curves in Figure 9h of BCCF, MoS_2/BCCF, Co-MoS_2/BCCF-21, and commercial RuO_2 indicated that Co-MoS_2/BCCF-21 catalyst can catalyze oxygen evolution at an onset potential of 1.45 V, which is only 0.06 V larger than RuO_2 (1.39 V), and better than MoS_2/BCCF. These results certified that covalent cobalt doping into MoS_2 could contribute to dramatically enhanced HER and OER activities. Figure 9i shows the optimized configuration of Co covalently doped MoS_2 and the calculated DOS, which exhibits the overlapped 3d states of Co with 3p states of its neighboring S atoms in MoS_2. The calculation illustrated that initial MoS_2 semiconductor possessed a bandgap of 1.70 eV, while the MoS_2 after Co doping possesses metallic characteristics with a bandgap (0 eV), which is quite beneficial for water splitting.

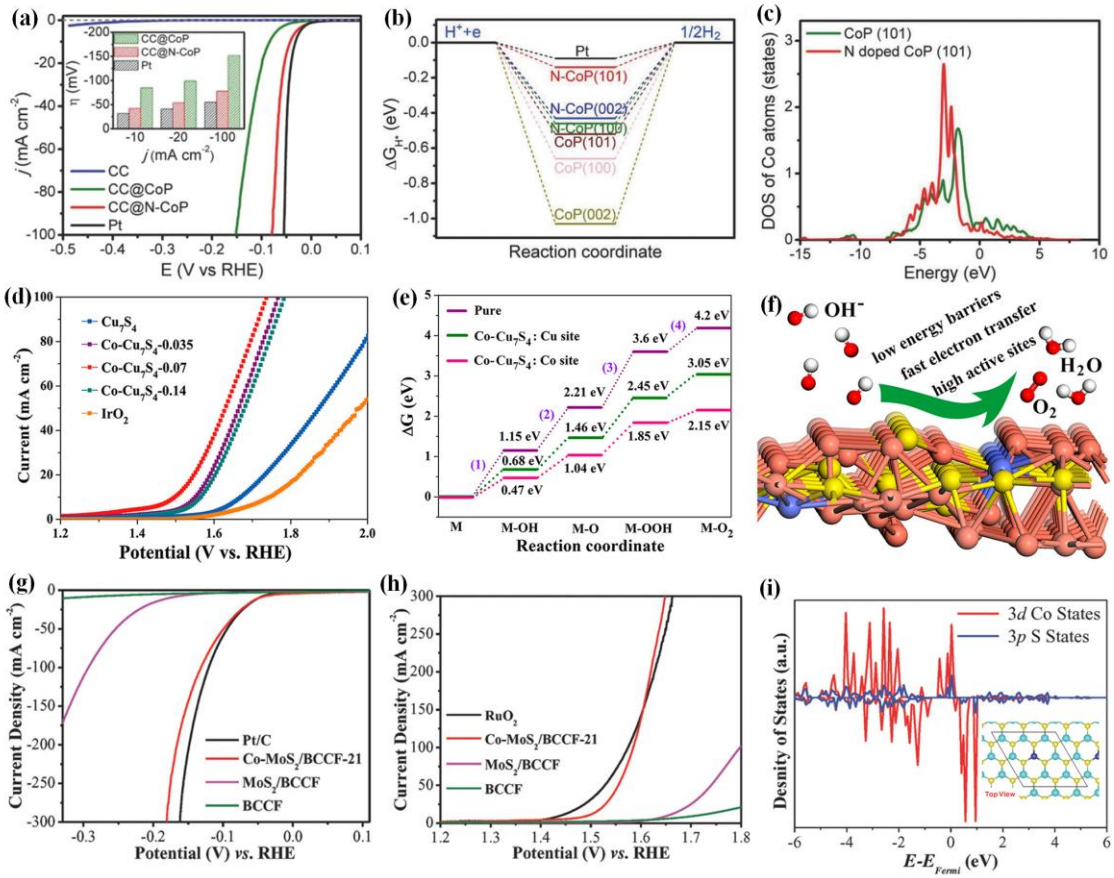

Figure 9. (a) The LSV curves for HER of CC, CC@CoP, CC@N-CoP, and Pt catalysts, (inset: corresponding η). (b) ΔG_{H^*} diagram at the Co–Co bridge site on the surfaces of CoP and N-CoP. (c) Calculated DOS of Co atoms on the CoP (101) surface with or without N doping. Reproduced with permission.[118] Copyright 2018, Wiley-VCH. (d) The LSV curves for OER of Cu_7S_4 and Co-Cu_7S_4 with different Co doping amounts. (e) Gibbs free energy diagram over pure Cu_7S_4, Cu site of Co-Cu_7S_4 and Co site of Co-Cu_7S_4. (f) The feasible OER mechanism for the Co engineered Cu_7S_4 catalyst. Reproduced with permission.[119] Copyright 2017, American Chemical Society. (g) The LSV curves for HER of BCCF, MoS_2/BCCF, Co-MoS_2/BCCF-21, and Pt/C electrodes and (h) LSV curves for OER of BCCF, MoS_2/BCCF, Co-MoS_2/BCCF-21, and RuO_2 electrodes. (i) Calculated DOS of 3d Co and 3p S states (insert: top views of the Co doped MoS_2 structure with a Mo/Co ratio of 8:1). Reproduced with permission.[120] Copyright 2018, Wiley-VCH.

Recently, single-atom doping has emerged as a promising strategy to tailor the

electronic structures, increase the electroactive site densities, facilitate electron transfer, and enhance corresponding stabilities of TM-based electrocatalysts for water splitting.[121-123] For example, Pt single atoms were introduced into VS_2 nanosheets via a cost-effective optothermal approach by Zhang et al., which can greatly boost the HER activities of VS_2.[124] In this work, the structures of Pt including single atoms (SAs), clusters and NPs on VS_2 nanosheets were well-controlled by optimizing the concentration of chloroplatinic acid. HAADF-STEM image (Figure 10a) and XAFS characterizations of as-prepared 0.1Pt/VS_2/CP electrode revealed that numerous atomically dispersed Pt were anchored on the VS_2 surface, and no Pt clusters or particles appeared. After Pt single atom doping, the HER performances of 0.1Pt/VS_2/CP were remarkably enhanced compared with those of pure VS_2/CP electrode. Figure 10b shows that the η_{10} of 0.1Pt/VS_2/CP electrode is 135 mV smaller than that of VS_2/CP. The mass activity of Pt/VS_2/CP with Pt SAs decorating was 12 times higher than Pt/C catalyst. DFT simulations revealed that Pt single atom doping on the VS_2/CP makes the ΔG_{H^*} value closer to zero (Figure 10c) and enhances the charge-transfer kinetics, significantly enhancing HER activity. Similarly, Xing and co-workers reported that Pd atom doping could chemically activate the molybdenum disulfide (MoS_2) surface basal plane for efficiently catalyzing HER.[125] Using a spontaneous interfacial redox method, Pd single atoms were doped at the Mo sites, which simultaneously introduced sulfur vacancy into MoS_2 due to the Mo redox process and transformed the 2H-MoS_2 into the stabilized 1T-MoS_2, which was proved by Figure 10d. K-edge EXAFS spectra and fitting curves (Figure 10e) shows that the Mo–S and Mo–Mo peak intensities of MoS_2 decreased after Pd doping, confirming the generation of sulfur vacancy and the rearrangement of Mo atoms. From Figure 10f, we can find that the MoS_2 doped with single Pd atoms displayed a lower η_{10} of 78 mV, compared with MoS_2 without Pd doping. DFT calculations revealed that the sulfur sites next to the Pd atoms exhibited low hydrogen adsorption energy. Calculated pDOS showed that S received electrons from the adjacent Mo atoms, leading to a weaker binding with hydrogen and higher HER activity. In addition, $Ni(OH)_2$ nanosheet electrocatalysts doped with atomically dispersed W for

OER catalysis were fabricated by Ma and his co-workers.[126] The atomically doping of W element and corresponding oxidized electronic structure (W^{6+}) of W were proved by XAS measurements and corresponding normalized XANES spectra. The HAADF-STEM image of the obtained sample in Figure 10g directly confirmed the single atom W in $Ni(OH)_2$ lattice according to these light spots from W element. Oxidation peaks of Ni^{2+} into $Ni^{3/4+}$ in LSV curves displayed a slight positive shift for the W-$Ni(OH)_2$ nanosheets, suggesting the single atom W doping could boost carrier migration. As shown in Figure 10h and 10i, the W-$Ni(OH)_2$ catalysts exhibited a lower η_{10} (237 mV) and a smaller Tafel slope value (33 mV dec^{-1}) than $Ni(OH)_2$. Theoretical results (Figure 10j) revealed that W^{6+} sites in $Ni(OH)_2$ matrix contributed to H_2O adsorption and O radical generation, suggesting that a single atom W could contribute to H_2O adsorption, generate adsorbed OH^- group and O radical, and further dramatically enhance the OER performances. Luo and his co-workers reported that Cr-doping could synergistically regulate H_2O and binding abilities over Co_4N, further resulted in exceptional HER performances in alkaline media.[127] Therefore, elemental doping has been widely used as is a promising method to increase the active site densities, tuning the electronic structures, optimize the adsorption of reactant species and reduce the related reaction barriers of various TM-based materials for efficient electrocatalysis.[128-139]

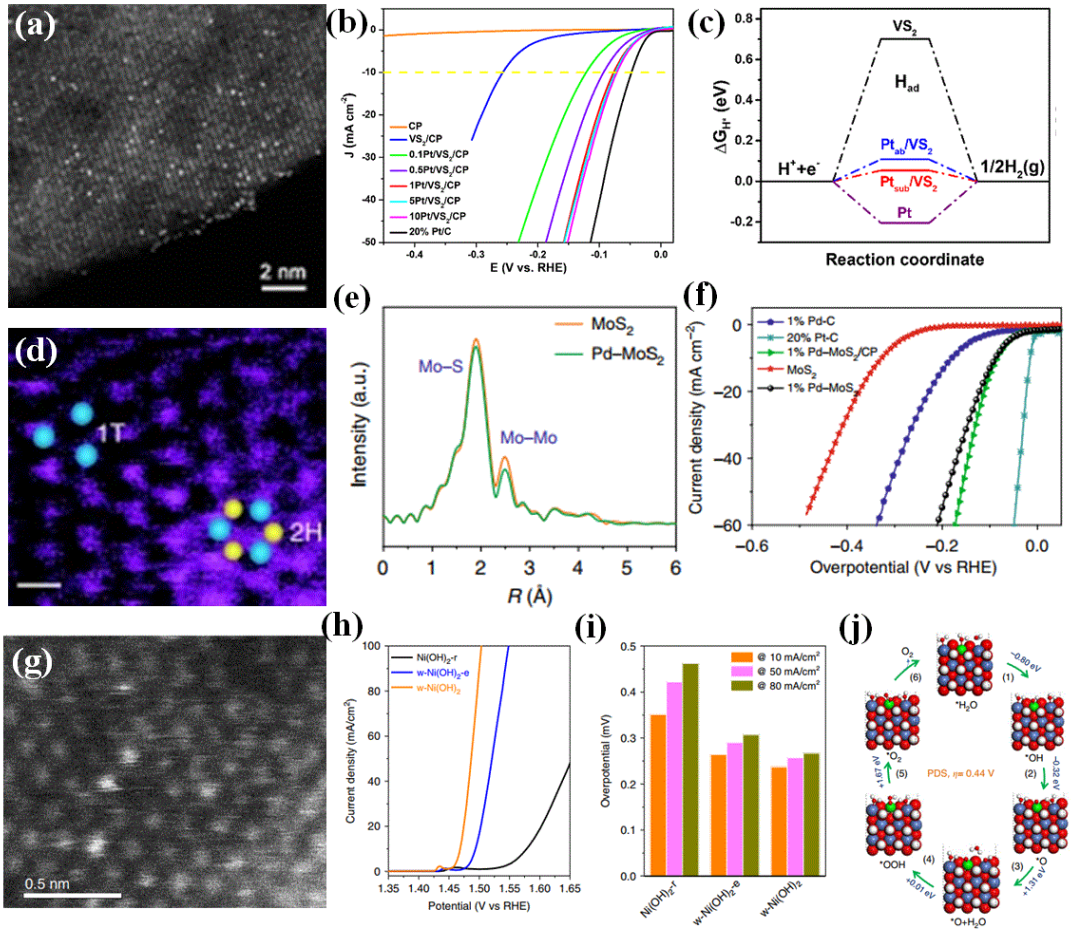

Figure 10. (a) HAADF-STEM image of single-atom Pt-decorated VS_2 nanosheets. (b) The LSV curves for HER of pure CP, pure VS_2/CP, different-amount Pt-decorated VS_2/CP and Pt/C. (c) ΔG_{H^*} diagram over pure VS_2, Pt_{sub}/VS_2, Pt_{ab}/VS_2, and Pt particles. Reproduced with permission.[124] Copyright 2020, American Chemical Society. (d) HAADF-STEM image of the 1%Pd–MoS_2 sample. Scale bar: 1 nm. Blue ball: Mo and yellow ball: S. (e) Fourier transform curves for Mo K-edge of the EXAFS spectra of MoS_2 and Pd-MoS_2. (f) The LSV curves for HER with iR correction in 0.5 M H_2SO_4 media. Reproduced with permission.[125] Copyright 2018, Nature Publishing Group. (g) HAADF-STEM image of single W-$Ni(OH)_2$ sample. (h) The LSV curves for OER with 95%-correction. (i) The η at current densities of 10, 50, 80 mA cm^{-2} over different electrodes. (j) Mechanism study of OER over W-doped $Ni(OH)_2$ by DFT calculations. Red, white, green, and blue ball: oxygen, hydrogen, nickel, and tungsten atom, respectively. Reproduced with permission.[126] Copyright 2019, Nature Publishing

Group.

3.5. Engineering by defects

The defects, including point defects, line defects, two-dimensional defects, and three-dimensional defects, could cause distortions of the structure in the crystalline solids, which further drastically change their electron distribution and band structure. Therefore, defect-engineering methods can play vital roles in regulating electrochemical water splitting activities and stabilities of TM-based electrocatalysts through regulating their conductivities, active site centers, and adsorption/desorption abilities. In this section, the roles of oxygen vacancy defects, cation vacancy defects, and multi-vacancy defects in improving the electrochemical reaction performances are carefully pointed out.

3.5.1. Engineering by oxygen vacancy defects

Oxygen vacancy, as one of the most common anion vacancies in the TM oxides has usually been created to regulate the electrocatalytic performances. Upon oxygen vacancies are introduced into TM oxide-based catalysts, the electronic structures could be greatly changed, and then the metal oxides can be transformed from a conventional semiconductor with low conductivity into a degenerate one with higher conductivity. These tuned electronic structures by oxygen vacancies could also reduce the reaction barriers of HER or OER and optimize the adsorption abilities of regent species over the catalysts, finally leading to enhanced catalytic performances. Therefore, introducing oxygen vacancies into TM-based oxides has been applied widely to directly and effectively tune the intrinsic electrocatalytic performances.[140-146] For instance, Zeng and his co-workers prepared WO_3 nanosheets with oxygen vacancies as HER catalysts.[147] DFT simulation predicted introducing oxygen vacancies into WO_3 can tune their electronic structures, improve their conductivities and optimize the hydrogen adsorption abilities. As depicted in Figure 11a, the DOS of bulk WO_3 without oxygen vacancy shows a typical semiconductor character, where Fermi level locates within band gap. Nevertheless, when oxygen vacancies are introduced, new energy levels

appear at conduction band minimum and its band gap is narrowed. Moreover, the Fermi level is located at the conduction band minimum of W 5d, suggesting the formation of a degenerate semiconductor. Moreover, the calculated ΔG_{H^*} diagram in Figure 11b displays that the ΔG_{H^*} value of perfect WO_3 is 2.3 eV, and when oxygen vacancies are introduced, the ΔG_{H^*} value is reduced and comparable to that of platinum. Experimentally, the as-prepared WO_3 nanosheets with oxygen vacancies exhibited excellent activities with a low η_{10} of 38 mV (Figure 11c) and a small Tafel slope of 38 mV dec^{-1}, implying that introducing oxygen vacancies could efficiently boost the HER performances. Shi and his co-workers reported a facile method to synthesize an effective HER electrocatalyst of Pt/def-WO_3@CFC with platinum atom clusters dispersed on oxygen vacancy-rich WO_3. For HER catalysis, this as-fabricated electrocatalyst exhibited Pt/C like performances, which were partly generated from oxygen vacancies in WO_3 nanoplates.[148] Moreover Zheng and his co-workers proposed a facile method to prepare Co_3O_4 nanowires with rich oxygen vacancies via the $NaBH_4$ aqueous solution-treatment at room temperature (Figure 11d).[149] XRD and XPS results confirmed the generation of oxygen vacancies in Co_3O_4 nanowires (NWs) after $NaBH_4$ treatment. The formation energy plots (Figure 11e) form DFT calculation shows that the Vo^{2+} possesses the lowest formation energy, suggesting oxygen vacancies are most likely formed as Vo^{2+}. The calculated total DOS and projected DOS (Figure 11f) indicate that Co_3O_4 NWs with oxygen vacancies are equipped with a new state within their band gap. In these sates, the electrons associated with the Co-O bonds become more delocalized, leading to higher electrical conductivity and better electrocatalytic performance than pristine Co_3O_4. The Co_3O_4 with oxygen vacancies exhibited enhanced OER performances compared with pure Co_3O_4, with a small onset potential of 1.52 V (Figure 11g), and a low Tafel slope of 72 mV dec^{-1} (Figure 11h). These experimental results confirmed that the oxygen vacancies in metal oxides could result in new gap states, dramatically improving the conductivity and boosting their electrocatalytic performances.

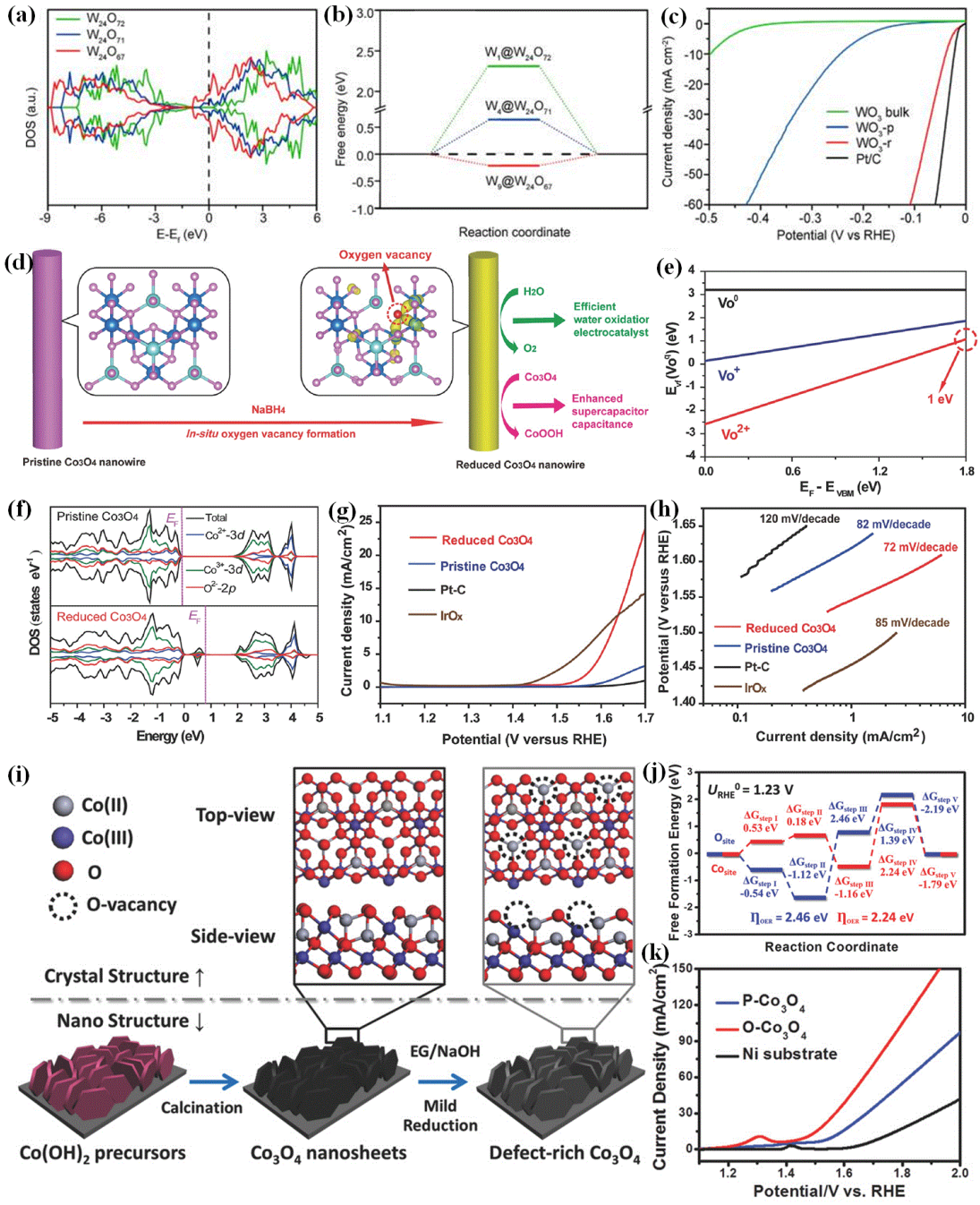

Figure 11. (a) The calculated partial DOS of W in WO_3 with different oxygen vacancies. (b) Free-energy diagram on WO_3 (010) face with oxygen vacancies. (c) LSV curves for HER of the WO_3 bulk, $WO_{3\text{-}p}$ NSs, $WO_{3\text{-}r}$ NSs and Pt/C. Reproduced with permission.[147] Copyright 2017, American Chemical Society. (d) Schematic illustration of introducing oxygen vacancy into Co_3O_4 NWs. (e) Calculated formation energies of Co_3O_4 with vacancies. (f) TDOS and PDOSs of the perfect Co_3O_4 and defective Co_3O_4. (g) LSV curves for OER of the Co_3O_4 NWs with/without defects, IrO_x and Pt/C in 1 M

KOH. (h) Tafel plots derived from LSV curves. Reproduced with permission.[149] Copyright 2014, Wiley-VCH. (i) Schematic illustration of introducing oxygen vacancies into single-crystalline Co_3O_4 nanosheets. (j) Free energy diagram over the Co_3O_4 configuration with/without oxygen vacancies. (k) LSV curves for OER of obtained Co_3O_4 with oxygen vacancy, pristine Co_3O_4 catalysts, and Ni substrate in 1 M KOH media. Reproduced with permission.[150] Copyright 2018, Wiley-VCH.

Afterwards, Sun et al. presented a solvothermal reduction approach (Figure 11i) with ethylene glycol as the reducing agent to create oxygen vacancies in the single-crystalline Co_3O_4 nanosheets.[150] Corresponding DFT calculation (Figure 11j) showed the lower OER activation energy value of 2.24 eV on Co_3O_4 nanosheet surface with oxygen vacancies (2.46 eV on pristine Co_3O_4), implying advantageous OER kinetic over defective Co_3O_4. The band gap fo pristine Co_3O_4 is 1.93 eV, while a narrow band gap of 1.74 eV was obtained after the creation of oxygen vacancies into Co_3O_4, confirming high conductivity of Co_3O_4 with oxygen vacancies. XPS and XANES experimental results confirmed that the oxygen vacancies were generated on the surface of Co_3O_4, and the lower Co coordination number of defected Co_3O_4 than that of pristine Co_3O_4 nanosheets endowed their high activities. The LSV curves in Figure 11k displays that the onset overpotential is lowered from 300 mV to 220 mV after introducing oxygen vacancies in to Co_3O_4. In addition, the defective Co_3O_4 with rich oxygen vacancies also exhibited smaller Tafel slope value (49.1 mV dec^{-1}) than perfect Co_3O_4 (72.3 mV dec^{-1}), implying a booted intrinsic activity by oxygen vacancies. Plasma engraving was also employed to create oxygen vacancies into metal oxide catalysts. For example, Wang and co-workers reported that Ar radiofrequency plasma treatment can generate oxygen vacancies in Co_3O_4 nanosheets.[151] After plasma treatment, the Co_3O_4 nanosheets possessed rough and discontinuous surfaces, resulting in larger active surface areas. Defect states within the band gaps of Co_3O_4 were detected by DFT calculation, confirming the high electrical conductivity. Owing to the optimized electronic structure and conductivity, the Ar-plasma engraved Co_3O_4 nanosheets exhibited better OER performances than pure Co_3O_4. These experimental and

theoretical results confirmed that oxygen vacancies are of great significance in improving water splitting performances of TM-based electrocatalysts through the following aspects: (1) work as active centers and increase the density of catalytic site; (2) improve their conductivity by the generation of new gap states or narrow the band gap; and (3) optimize the adsorption/desorption ability of regent species and lower the reaction barriers.[152-155] Therefore, it is desired to develop additional facile strategies and implement these strategies to precisely engineer the density and distribution of oxygen vacancies in metal oxides-based electrocatalysts to dramatically boost their catalytic performances.

3.5.2. Engineering by cation vacancy defects

As another kind of classical defects, cation vacancy could effectively regulate the surface electronic properties of host catalysts, increase their active sites, and accelerate charge transfer, further promote the reaction kinetics, and reduce the reaction barriers. Compared with oxygen vacancy, metal cation vacancy possesses higher formation energy, but with the rapid improvement of advanced characterization and synthetic technology, engineering the catalytic performances via cation vacancy for efficiently catalyzing HER or OER has attracted attention.[156,157] For instance, Chen and his co-workers synthesized a nanocrystalline $Co_xMn_{3-x}O_4$ catalyst with abundant metal (Co or Mn) cation vacancies.[158] DFT calculations revealed that this spinel $Co_xMn_{3-x}O_4$ catalyst with metal cation vacancies exhibited optimized electronic states, leading to favorable oxygen-binding abilities. Experiment results showed that the as-prepared $Co_xMn_{3-x}O_4$ catalyst possessed superior catalytic activities toward the OER. Messinger and co-workers reported that Fe vacancies could be introduced into FeP by chemical leaching of Mg and as-obtained Fe vacancy-rich FeP nanoparticulate exhibited superior HER performances to FeP and Mg-doped FeP, possessing η_{10} of 65 mV in 0.5 M H_2SO_4. The theoretical and experimental analyses demonstrated that Fe vacancies could regulate electronic structures, optimize hydrogen adsorption, as well as contribute to proton trapping, dramatically improving HER activities.[159] Besides, ultrathin feroxyhyte (δ-

FeOOH) nanosheets with Fe vacancies-defect were designed and the optimized structure of δ-FeOOH is shown in Figure 12a.[160] Figure 12b and 12c show the HER and OER performances of defective δ-FeOOH and reference samples in 1 M KOH solution, which clearly demonstrated the enhanced water splitting performances of Fe vacancies-defect δ-FeOOH and theoretical results confirmed that active sites are neighboring Fe atoms to Fe vacancies. In addition, cobalt-defected $Co_{3-x}O_4$ as OER catalysts was *in situ* prepared by Zou and co-workers.[161] The generation of Co vacancies and distortion structures of prepared $Co_{3-x}O_4$ were characterized by XAFS and positron annihilation lifetime spectra (PALS), and the tuned electronic structures of Co-defected $Co_{3-x}O_4$ were studied by DFT. As shown in Figure 12d, the $Co_{3-x}O_4$ possessed an increased DOS for the occupied states from 0.50 eV above the Fermi level and a smaller bandgap with respect to Co_3O_4. The presence of Co vacancies could result in distortion to neighboring atoms and electronic delocalization, which are beneficial for faster charge transport during water splitting reactions. Figure 12e displays the process of H_2O adsorption on Co_3O_4 and $Co_{3-x}O_4$ surfaces. The hydrogen atom of H_2O molecule was drawn to surface oxygen nearby adsorbed Co site on $Co_{3-x}O_4$, and the adsorbed energy of H_2O is − 1.07 eV, lower than that on normal Co_3O_4 (− 0.98 eV), suggesting Co vacancies could contribute to H_2O adsorption during OER process. As predicted, remarkably high OER performances were obtained with the cobalt-defected $Co_{3-x}O_4$ as electrocatalysts (Figure 12f), which deliver a lower η_{10} of 268 mV than normal Co_3O_4 (376 mV) in 1 M KOH solution. Additionally, Liu and co-workers proposed metal-vacancy-solid-solution NiAlP, which could be employed as bifunctional electrocatalysts for all-pH HER and OER.[162] The EDS, ICP, XPS and HRTEM image (Figure 12g) confirmed the formation of Al vacancies in NiAlP after alkali-etching treatment. Figure 12h displays the NiAlP nanowall array with abundant Al vacancies possessed much higher HER performances with a low η_{10} of 35 mV. However, an overpotential of 78 mV is needed to achieve 10 mA cm^{-2} over NiAlP, confirming the enhanced intrinsic HER activity of the defective NiAlP was originated from Al vacancies. In addition, the NiAlP nanowall array with abundant Al vacancies exhibited a smaller Tafel slope of 38 mV dec^{-1}, that

is very close to commercial Pt/C (30 mV dec^{-1}) and superior to NiAlP (89 mV dec^{-1}). Similarly, improved OER performances were also obtained when using Al vacancies-defect NiAlP as the catalyst as shown in Figure 12i, where a lower η_{10} of 256 mV and a smaller Tafel slope of 76 mV dec^{-1} were obtained, which are much better than NiAlP sample without vacancies. Moreover, the as-prepared Al-vacancies defect-rich NiAlP nanowall arrays exhibited outstanding water spltting activities, needing low cell voltages of 1.50–1.70 V to reach 10 mA cm^{-2} under pH of 0–14. Furthermore, the calculated band structure of NiAlP with Al vacancies (Figure 12j) displays high charge densities distributed around the Fermi level, which is greater than that of perfect NiAlP, suggesting that the introduced Al-vacancies sped up the electron transfer during reactions. The partial charge density (Figure 12k) shows that Al vacancies could enhance the electrons delocalization, leading to more efficient centers toward water electrocatalysis. The ΔG_{H^*} and H_2O adsorption energy plots (Figure 12l) indicated that the surface with Al vacancies is beneficial to proton and O-related species adsorption. The results manifested that well-designed metal vacancies in electrocatalysts could optimize the electronic properties and provide more active centers, thus endowing catalysts with excellent activities toward both HER and OER. Accordingly, it is crucial to design facile methods to create cation vacancies into TM-based electrocatalysts and make efforts to explore the relationship between cation vacancies and electronic structures.[163-166]

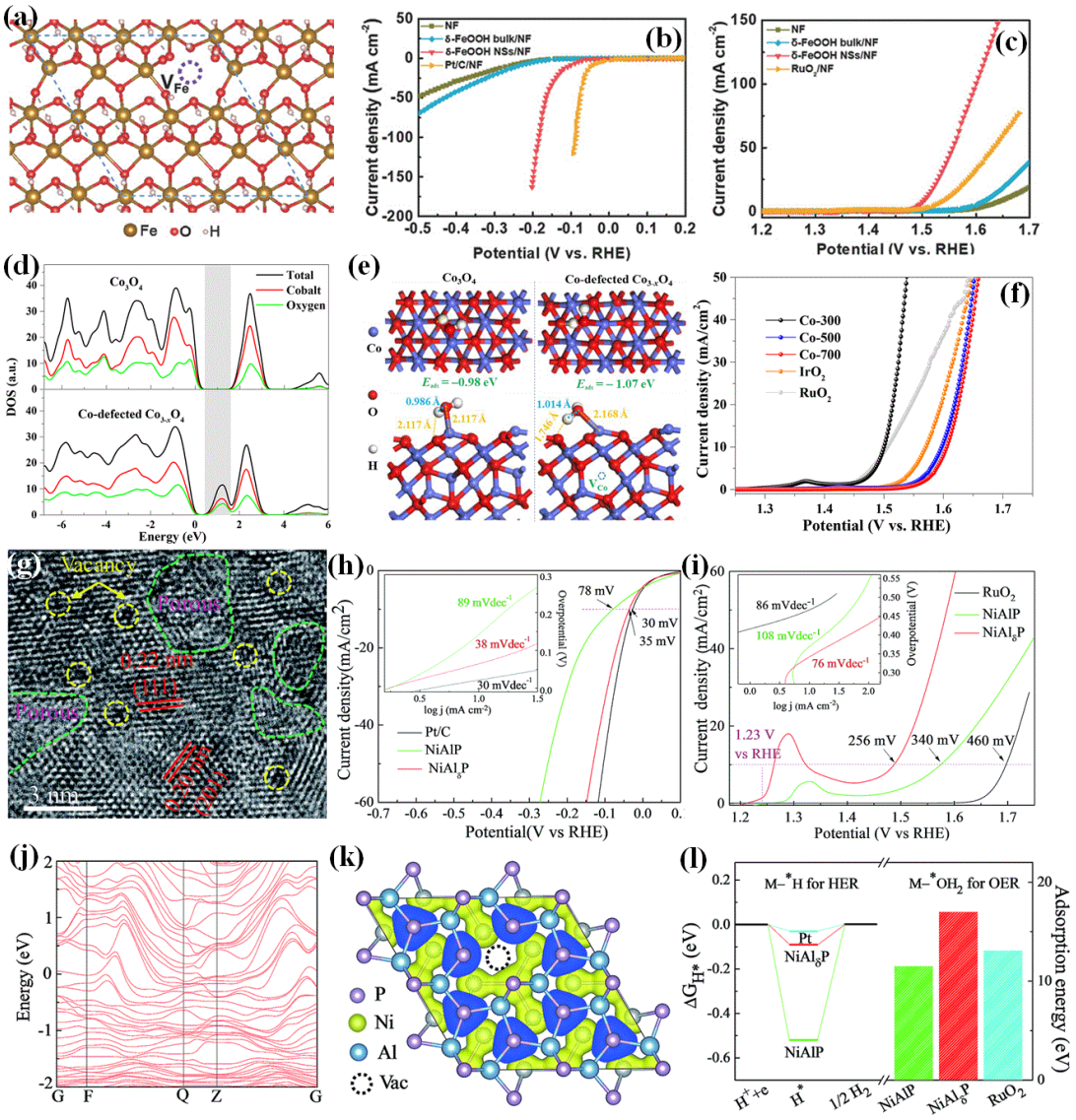

Figure 12. (a) The optimized structure of δ-FeOOH with Fe vacancy. (b) The LSV curves for HER and (c) LSV curves for OER in 1.0 M KOH electrolyte. Reproduced with permission.[160] Copyright 2018, Wiley-VCH. (d) Calculated total and projected DOS of Co_3O_4 and Co-defected $Co_{3-x}O_4$. (e) Optimized configurations of H_2O adsorbed on (111) surface of Co_3O_4 (top and site views, (left) and Co-defected $Co_{3-x}O_4$ (right). (f) LSV curves for OER of $Co_{3-x}O_4$ samples calcined at 300, 400 and 500 °C (denoted as Co-300, Co-500, Co-700), IrO_2 and RuO_2 samples in 1 M KOH solution. Reproduced with permission.[161] Copyright 2018, American Chemical Society. (g) HRTEM image of obtained NiAlP with Al vacancies. (h) The HER and (i) OER performances of NiAlP nanowall array with/without Al vacancies. Insets: the corresponding Tafel plots. (j) The

calculated band structure of NiAlP with Al vacancies. (k) The local charge density of NiAlP with Al vacancies. (l) The calculated ΔG_{H^*} diagram and H_2O adsorption energy values over NiAlP, NiAldP with Al vacancies and Pt or RuO_2. Reproduced with permission.[162] Copyright 2018, Royal Society of Chemistry.

3.5.3. Engineering by multi-vacancies defects

As mentioned above, both anion and cation vacancy can efficiently engineer the electronic structures of TM-based materials to improve their electrocatalytic performances. Therefore, introducing multi-vacancies with different types into nanomaterials could also be a promising strategy to greatly tune their electrocatalytic activities. For example, Fan and co-workers reported fluorine could induce dual defects (F-anion doping and P vacancy) into cobalt phosphide nanosheets and then the dual defects can greatly boost the electrocatalytic performances.[167] The successful formation of dual defects in CoP nanosheets was proved by in situ depth XPS and EXAFS spectra. In Figure 13a, peaks with binding energies of 782.3 eV and 798.4 eV are ascribed to Co^{2+}, which is generated from the ionic Co^{2+}-F and Co^{2+}-O bonds. The F 1s spectrum (Figure 13b) also confirms the appearance of F-Co bonds (peak at 685.5 eV), which clearly proves the successful introduction of F atoms into the CoP nanosheets. In Figure 13c, the absorption edge of CoP with F doping and P vacancy (denoted as F-CoP-V_p) located at a higher energy than pure CoP, confirming a increased valence state of Co in F-CoP-V_p due to the electronegative F atoms incorporation. In addition, the corresponding fitting curves confirm the formation of P vacancies in F-CoP-V_p sample. DFT calculation revealed that the F doping could result in easier adsorption of water molecular and P vacancies could make the ΔG_{H^*} reduced closer to zero (Figure 13d). Meanwhile, the obtained charge density distribution revealed that F doping can trigger localization of charge density distribution and further increase electrical conductivity. As a result, the dual defects lead to nearly 15-fold enhancement toward experimentally catalytic HER in neutral media (Figure 13f). Wang and co-workers presented a simple

approach (Figure 13g) to introduce multiple vacancies (Co, Fe and O vacancies) into 2D CoFe LDHs (denoted as E-CoFe LDHs) by acid-base reaction, which finally leaded to significantly enhanced OER performances.[168] To prove the successful generation of multi vacancies defects and investigate the tuned electronic structures by multi vacancies, XAS was employed. Figure 13h and 13i shows coordination environment changes of Co and Fe atom caused by defects. The Fourier transform (FT) of EXAFS curves for Co K-edge (Figure 13j and 13k) displays Fe-O and Fe-Co coordination peaks largely decreased after acid etching, confirming the appearance of oxygen vacancies and iron vacancies. Figure 13l shows the catalytic LSV curves, where the E-CoFe LDHs with multi vacancies defects exhibited higher OER performances than perfect CoFe LDHs. Besides, Ar plasma etching was employed to convert the bulk CoFe LDHs into monolayer nanosheets, and abundant Co, Fe, and O vacancies were created at the same time.[169] These introduced multi vacancies defects (O, Co, and Fe vacancies) led to more exposed active sites and dramatically enhanced their intrinsic electrocatalytic activities of 2D CoFe LDHs nanosheets. Similarly, a water-plasma-enabled exfoliation method was also employed to introduce O, Co, and Fe vacancies into CoFe LDH for water oxidation.[170] Moreover, Cai and co-workers presented an efficient neutral water electrolyzer material based on LDH with O, Ni, and Fe multiple vacancy defects. Because of these multiple vacancy defects, the prepared NiFe LDH possessing improved electrical conductivity and faster charge transfer, displayed a small η_{10} of 87 mV for HER in a pH 7 buffer electrolyte.[171]

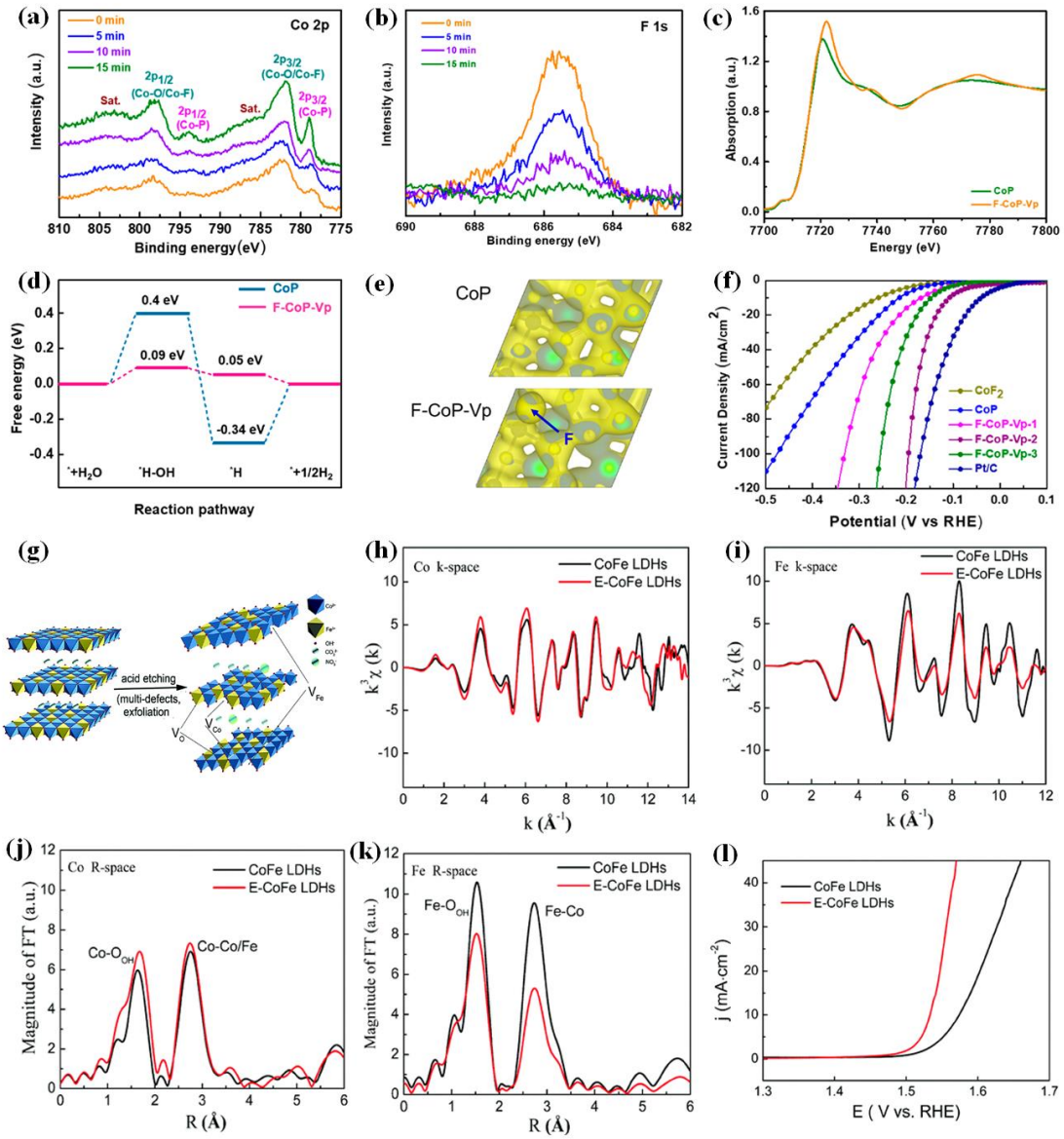

Figure 13. The in situ depth Co 2p (a) and F 1s (b) XPS patterns in F-CoP-V_{p-2} nanosheets. (c) Co Kedge XANES spectra of the F-CoP-V_{p-2} nanosheets. (d) Reaction pathways of HER over the (211) surfaces of CoP and F-CoP-V_p. (e) Charge density distribution of CoP (top) and F-CoP-V_p (bottom). (f) The LSV curves for HER of commercial Pt/C, CoF_2, CoP and F-CoP-V_p samples in 1 M PBS electrolyte. Reproduced with permission.[167] Copyright 2020, American Chemical Society. (g) The process of synthesizing CoFe LDHs with O, Co and Fe multi-vacancies. (h) Co and (i) Fe K-edge extended XANES oscillation functions $k_3\chi(k)$ of FeCo LDHs and E-FeCo LDHs with multi-vacancies. (j) Co and (k) Fe K-edge Fourier transform magnitudes of EXAFS. (l) LSV curves of FeCo LDHs and E-FeCo LDHs for OER in the alkaline

electrolyte. Reproduced with permission.[168] Copyright 2017, Royal Society of Chemistry.

3.6. Other strategies for engineering electrocatalysts

Besides aforementioned strategies, some others have also been employed to engineer the electronic structures of TM-based materials to further enhance their electrocatalytic performances. Varying the particle size of catalysts could regulate their electronic structures and lead to more active centers. For example, Behm and co-workers explored the dependence of HER performances on the Pt NC sizes. A volcano-like relationship between activities and sizes was obtained, and Pt NCs with ca. 38 atoms displayed highest j_0.[172] Zeng and co-workers designed a facile approach to boost the OER performances of perovskite cobaltite $LaCoO_3$ through reducing the particle size.[173] Tuning the sizes of $LaCoO_3$ could efficiently engineer their e_g filling, leading to the transform from low-spin to high-spin sates of Co ions and more active sites at the surfaces. When the average sizes of $LaCoO_3$ particles were reduced to approximately 80 nm, e_g filling of Co reached to optimal value of 1.2 and their OER performances were dramatically enhanced compared with $LaCoO_3$ bulks. Moreover, when the size of catalysts decreased to single atom level, the utilization efficiency of metal centers and the number of exposed active sites can be significantly changed, consequently regulating the electrocatalytic activities. For example, Allen J. Bard and co-workers investigated the size effects on the HER using the single-Pt atoms, Pt clusters, and Pt NPs as examples, where the HER kinetics increased with size increasing (0.2 ~ 4 nm) and reached the limitation of activity.[174] Wang and co-workers synthesized single-atom Pt anchored onto N-doped porous carbon with Pt loading of 3.8 wt% via a photochemical solid-phase reduction approach.[175] As-prepared Pt_1/NPC catalyst exhibited ultrahigh electrocatalytic performances toward HER with a low η_{10} of 25 mV and its mass activity was 24-times better than Pt/C catalyst.

The lattice tensile strain could also be useful to regulate electronic structures of TM-based catalysts and boost their electrocatalytic performances. For example, Guo et al.

presented that Co_9S_8/MoS_2 core/shell nanocrystals with precisely tuned tensile surface strain exhibited greatly boosted HER activities. The tensile strain of Co_9S_8/MoS_2 can change from 3.5% to 0% through tuning shell layers of MoS_2 and the Co_9S_8/MoS_2 sample with tensile strain of 3.5% displayed the best HER performances.[176] DFT calculation confirmed that the optimal Co_9S_8/MoS_2 nanostructure possessed the lowest reaction barrier of 0.29 eV and H adsorption energy of -1.03 eV due to the lattice tensile strain effects. Li and his co-workers employed the compressive strain to construct IrO_x layers on IrCo nanodendrites.[177] In situ EXAFS showed that its compressive strain could be tuned from 2.51% to unstrained state, which further led to variations in electrocatalytic OER activities. DFT calculations showed that the optimized strain can optimize the adsorption ability and promote the generation of HOO* species. Experimental results revealed that IrO_x with three layers on IrCo (approximately 1.51% strain), showed the best OER performances with a small η_{10} of only 247 mV in acid solution. Furthermore, Liu and co-workers reported that lattice tensile strain could engineer the anti-bonding filling states of the d orbital in NiFe hydroxide and boost oxygenated intermediates adsorption, thus dramatically boosting the water oxidation performances.[178] Moreover, Liu et al. reported that lattice-strained NiFe metal–organic frameworks (MOFs) showed much better activities than pristine NiFe MOFs.[179] Therefore, engineering the lattice tensile strain is a facile and potential strategy to regulate their electronic structures and optimize their adsorption abilities of TM-based catalysts for efficient electrocatalysis.

Controlling the coordination structure can also regulate the electron densities around TM sites, enhance electronic conductivity, and increase the exposed active sites of catalysts. For example, Xie and her co-workers revealed that coordination number of Co ions can be reduced from 5 to 3 by introducing pores in the surfaces of Co_3O_4 nanosheets.[180] The Co^{3+} sites could work as chemically catalytic OER centers and enhance conductivity through increasing DOS at the band edge. Consequently, the as-prepared porous Co_3O_4 atomically thick sheets displayed an electrocatalytic OER current density of 341.7 mA cm^{-2} at 1.0 V, approximately 50-times higher than Co_3O_4

bulks. Afterward, a heterostructure electrocatalyst containing low-coordinate IrO_2 confined on graphitic carbon nitride (GCN) was reported.[181] The coordination number of Ir atoms could result in lattice strain, further increase the electron densities around Ir sites, and optimize the adsorption ability of intermediates over the surfaces, thus greatly boosting the electrocatalytic performances. Besides, Fei et al. reported that Co–N linkage in Co–N–C catalyst could contribute to better performances towards HER.[182] Cao et al. synthesized Co-based HER catalyst by embedding Co atoms into P-doped g-C_3N_4, which exhibited a η_{10} of 89 mV in 1 M KOH.[183] In addition, Sa et al. synthesized HER catalysts with Co–N_x moieties supported onto CNT, in which the coordination structure of pyridine-type Co–N_4 showed best performance.[184] Consequently, controlling the coordination structure of TM-based electrocatalyst could be another effective strategy for engineering their electronic structures and greatly booting their electrocatalytic activities.

Table 2. Summary of the strategies used to enhance catalytic activities of TM-based electrocatalysts.

Strategies	Catalysts	Reaction	Electrolyte	η_{10} (mV)	Tafel Slope (mV dec^{-1})	Reference
Support Effects	Mo_2C@NPC	HER	0.5 M H_2SO_4	260	126.4	*Nat. Commun.* **2016**, *7*, 11204.
	Mo_2C@NPC/NPRGO			34	33.6	
	FeCo alloy in Graphene Layer	HER	1.0 M KOH	149	77	*ACS Catal.* **2017**, *7*, 469.
	RuCo@NC	HER	1.0 M KOH	28	31	*Nat. Commun.* **2017**, *8*, 14969.
	Pure $CoSe_2$	OER	0.1 M KOH	484	66	*ACS Nano* **2014**, *8*, 3970.
	NG-$CoSe_2$			366	40	
	$Co_3(PO_4)_2$	OER	1.0 M KOH	-	103	*J. Mater. Chem. A* **2016**, *4*, 8155.
	$Co_3(PO_4)_2$@N-C			317	62	
	FeOOH	OER	1.0 M KOH	-	101	*Adv. Energy Mater.* **2018**, *8*, 1702598.
	FeOOH/NPC			-	33.8	

Interface Effects	Ni_3N/Ni/NF	HER	1.0 M KPi	19	-	*Nat. Commun.* **2018**, *9*, 4531.
			1.0 M KOH	12	29.3	
	GC/TaS_2	HER	0.5 M H_2SO_4	267	89	*ACS Nano* **2019**, *13*, 11874.
	CF/TaS_2			186	73	
	Mo/TaS_2			110	58	
	Au/TaS_2			101	53	
	W_xC@WS_2-10	HER	0.5 M H_2SO_4	156	75	*Adv. Funct. Mater.* **2017**, *27*, 1605802.
	W_xC-60			192	68	
	WS_2			318.7	110	
	W_2N/WC	OER	1.0 M KOH	320	94.5	Adv. Mater. **2020**, *32*, 1905679.
Crystal Faces	Ni_3S_2/NF	HER	1.0 M KOH	223	-	*J. Am. Chem. Soc.* **2015**, *137*, 14023.
		OER		260	-	
	Co_3O_4-NC/N-rGO	OER	1.0 M KOH	440	124	*Adv. Energy Mater.* **2018**, *8*, 1702222.
	Co_3O_4-NTO/N-rGO			410	78	
	Co_3O_4-NP/N-rGO			380	62	
	{110} faces exposed Co_3O_4 nanosheets	OER	1.0 M KOH	318	66	*ACS Appl. Mater. Interfaces* **2018**, *10*, 7079.
	{111} faces exposed Co_3O_4 nanosheets			339	69.4	
	{112} faces exposed Co_3O_4 nanosheets			320	57.6	
	Bulk TaC	HER	0.5 M H_2SO_4	> 400	232	*Nano Energy* **2017**, *36*, 374.
	TaC NCs@C			146	143	
Elemental Doping	CC@CoP	HER	0.5 M H_2SO_4	85	50.5	*Adv. Mater.* **2018**, *30*, 1800140.
	CC@N-CoP			42	41.2	
	Cu_7S_4	OER	1.0 M KOH	510	197	*ACS Nano* **2017**, *11*,

	Co-Cu_7S_4-0.07			270	130	12230.
	Co-MoS_2/BCCF-21	HER	1.0 M KOH	48	52	*Adv. Mater.* **2018**, *30*, 1801450.
		OER		260	85	
	VS_2/CP	HER	0.5 M H_2SO_4	257	125.87	*ACS Nano* **2020**, *14*, 5600.
	1Pt/VS_2/CP			77	40.13	
	MoS_2	HER	0.5 M H_2SO_4	328	157	*Nat. Commun.* **2018**, *9*, 2120.
	1% Pd-MoS_2/CP			89	32	
	$Ni(OH)_2$-r	OER	1.0 M KOH	351	111	*Nat. Commun.* **2019**, *10*, 2149.
	w-$Ni(OH)_2$-e			264	58	
	w-$Ni(OH)_2$-e			237	33	
	Co_4N	HER	1.0 M KOH	150	128	*Adv. Energy Mater.* **2019**, *9*, 1902449.
	Cr-Co_4N			21	38.1	
Defects	WO_{3-p} NSs	HER	0.5 M H_2SO_4	245	78	*Nano Lett.* **2017**, *17*, 7968.
	WO_{3-r} NSs			38	38	
	Pristine Co_3O_4	OER	1.0 M KOH	-	82	*Adv. Energy Mater.* **2014**, *4*, 1400696.
	Reduced Co_3O_4			-	72	
	P-Co_3O_4	OER	1.0 M KOH	-	72.3	*Adv. Energy Mater.* **2018**, *8*, 1701694
	O-Co_3O_4			-	41.9	
	Pristine Co_3O_4	OER	0.1 M KOH	540	234	*Angew. Chem., Int. Ed.* **2016**, *55*, 5277.
	plasma engraved Co_3O_4 (120s)			300	68	
	δ-FeOOH NSs/NF	HER	1.0 M KOH	108	68	*Adv. Mater.* **2018**, *30*, 1803144
		OER		265	36	
	$Co_{3-x}O_4$	OER	1.0 M KOH	268	38.2	*ACS Catal.* **2018**, *8*, 3803.

	NiAlP	HER	0.5 M H_2SO_4	78	89	*J. Mater. Chem. A* **2018**, *6*, 9420.
		OER		340	108	
	$NiAl_\delta P$	HER		35	38	
		OER		256	76	
	CoP	HER	1.0 M PBS	215	123.2	*ACS Materials Lett.* **2020**, *2*, 736.
	F-CoP-Vp-2			108	88.9	
	CoFe LDHs-Ar	OER	1.0 M KOH	266	37.85	*Angew. Chem. Int. Ed.* **2017**, *56*, 5867.
	E-CoFe LDHs	OER	1.0 M KOH	300	41	*Chem. Commun.* **2017**, *53*, 11778.

4. Reaction Mechanisms

Generally, electrocatalytic water spltting occurs at the interfaces between electrocatalysts and electrolyte, which involve the absorption of reactants onto the catalyst surfaces, the migration of intermediate species, and the desorption of produced gases, indicating that the intrinsic electronic structures of the catalysts can determine its electrocatalytic performances.[185-188] Based on the above-detailed discussions about the TM-based electrocatalysts, we drew the corresponding conclusion about the structure–performance relationships that the structures/compositions of materials determine their intrinsic electronic structures, and further alter the reaction mechanisms and catalytic performances. Moreover, these strategies summarized in this review could efficiently engineer the electronic structures of TM-based electrocatalysts to improve their conductivities, increase active sites, optimize adsorption/desorption abilities, and reduce reaction barriers, leading to enhanced performances towards hydrogen or

oxygen evolution reactions. For example, support effects could improve conductivity and accelerate charge transfer by regulating electronic structures of active materials, further greatly improving the electrocatalytic performances. Interface effects and crystal face tuning strategies could increase the active sites and regulate the intrinsic sites by engineering their electronic structures, leading to enhanced catalytic performances. Elemental doping and defects tuning strategies could improve the conductivity, increase the active site densities, optimize the adsorption of reactant species, and reduce the related reaction barriers by regulating the electronic structures of TM-based catalysts. Consequently, it is imperative to deeply explore the mechanism of water splitting reactions and carefully analyze the relationship between structures and performances of TM-based electrocatalysts.

Recently, operando analysis has been employed as useful methods for providing profound insights into the underlying reaction mechanisms.[189-194] For example, Liu et al. utilized in situ XANES and EXAFS to study active sites and the dynamic variation of electronic configuration over hierarchical binary Ni–Co oxide catalyst during water oxidation.[195] The generation of NiOOH was demonstrated by in situ EXAFS spectra and the oxidation of Ni during OER was confirmed by operando EXAFS spectra, suggesting NiOOH worked as active site. Wang et al. explored the nature of high OER performances of state-of-the-art multi-metal oxides/(oxy)hydroxides at the atomic level using in-situ XAS.[196] A short V-O bond was detected during OER by in-situ X-ray absorption spectroscopic, suggesting V atoms can greatly contribute to the OER activity. Moreover, Schmidt and co-workers decoupled the activity losses towards high surface

area iridium oxides using operando X-ray characterization, making it possible to expound degradation mechanisms of OER.[197]

5. Conclusions and outlook

In this review paper, previously reported strategies of engineering TM-based catalysts to improve their electrocatalytic oxygen or hydrogen evolution activities were summarized and shown in Figure 14, which are crucial in ameliorating global energy and environmental issues. These strategies including support effects, interface effects, crystal face tuning, elemental doping, and defect tuning could remarkably regulate the electronic structures of TM-based nanomaterials and enhance their electrocatalytic activities as shown in Table 2. Nonetheless, developing facile methods of engineering various TM-based catalysts for excellent electrochemical H_2 production to replace the fossil fuels and deeply understanding the catalytic mechanism are still at an immature stage. Several aspects that further attention should be devoted to are listed below.

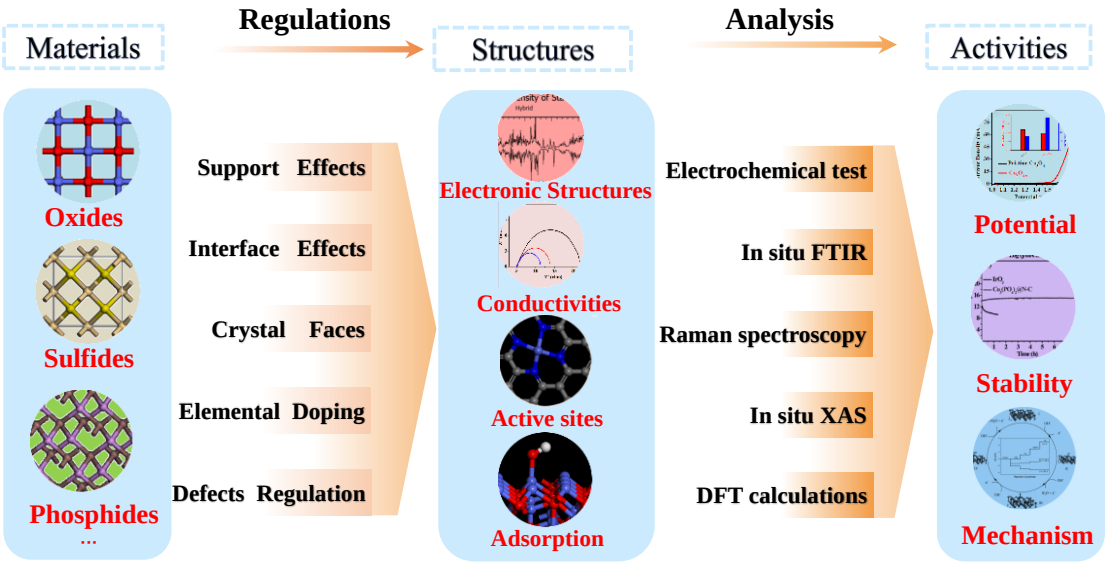

Figure 14. Perspective: potential strategies of engineering transition metal-based materials for H_2 production via water splitting.

(I) Currently, various TM-based materials with different intrinsic electronic

structures have been prepared as powerful electrocatalysts for HER and OER, however, ideal catalysts are still yet to be realized to replace commercial noble metal catalysts.[198-205] Thus, fundamentally designing novel TM-based materials with fine electronic structures and deeply understanding their electronic structure–property relationships need to be intensively explored.

(II) The mentioned strategies of engineering electrocatalysts in this review paper could work as useful methods in engineering the intrinsic electronic structures and boosting the catalytic performances of TM-based electrocatalysts. Therefore, these strategies should be continuously focused on until ideal electrocatalysts with excellent catalytic performances and stabilities are realized. Moreover, other effective and novel strategies, such as electric or magnetic fields tuning, electrolyte tuning, are also expected to greatly engineer electrocatalysts, further dramatically boosting their catalytic water splitting activity.

(III) The in-depth fundamental studies of regulated electronic structures, active centers and tuned catalytic activities need to be intensively explored using advanced characterization methods or in situ testing techniques or DFT calculations to understanding the structure-property relationship. The obtained structure–property relationship can be used to provide scientific guidance for optimizing the electrocatalysts. Advanced techniques such as in situ Raman spectroscopy, Fourier Transform Infrared Spectrometer (FTIR), X-ray absorption spectroscopy (XAS), and Molecular Dynamics simulation, as well as experimental techniques combined with computational simulations should be employed to propose deep insights into the electronic structures.

(IV) Pushing the low-cost and efficient electrocatalysts into large-scale industrial application even at harsh electrolyte conditions or very high/low potentials must be considered. The currently reported electrocatalysts were usually tested in the laboratory under mild condition, and the long-term stability is insufficient. Thus, designing or engineering the catalysts to make them more active and preserve these active sites at extreme electrolyte or potential conditions for clean energy generation at a much larger

scale is urgent and requires further research.

Notes

The authors declare no competing financial interest.

Biographies

Cheng-Zong Yuan received his Ph.D. degree from University of Science and Technology of China in 2019. He is currently a postdoctoral researcher at University of Macau. His research interests focus on designing nanomaterials for energy storage and conversion, such as water splitting, metal-air battery, and CO_2 electroreduction.

Kwan San Hui is a Reader in Mechanical Engineering of School of Engineering, University of East Anglia. He obtained his Ph.D. degree in mechanical engineering at the Hong Kong University of Science and Technology (2008). His research focuses on advanced materials for energy storage, conversion and electrocatalysis.

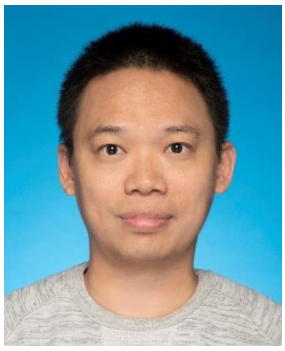

Fuming Chen is a Professor of School of Physics and Telecommunication Engineering, South China Normal University (SCNU). He received his Ph.D. from the Nanyang Technological University at Singapore in 2010. His current research interests are focused on advanced functional materials for electrochemical energy storage and desalination.

Kwun Nam Hui is an Associate Professor of Institute of Applied Physics and Materials Engineering, University of Macau. He obtained his Ph.D. degree from The University of Hong Kong (2009). His research focuses on electrochemical energy storage and conversion.

Acknowledgements

This work was funded by the Science and Technology Development Fund, Macau SAR (File no. 0191/2017/A3, 0041/2019/A1, 0046/2019/AFJ, 0021/2019/AIR), University of Macau (File no. MYRG2017-00216-FST and MYRG2018-00192-IAPME), the UEA funding, Zhejiang Province Basic Public Welfare Research Project (LGF19B070006), Science and Technology Program of Guangzhou (2019050001), National Key Research and Development Program of China, the Scientific and Technological Plan of Guangdong Province (2018A050506078, 2018B050502010), the Department of Education of Guangdong Province (2019KZDXM014, 2018KTSCX047), China Postdoctoral Science Foundation (2019M662955), Natural Science Foundation of Guangdong province (2019A1515011615), SCNU Outstanding Young Scholar Project (8S0256). C. Z. Yuan acknowledges the UM Macao Postdoctoral Fellowship and Associateship. F. Chen acknowledges the Pearl River Talent Program (2019QN01L951).

References

(1) Turner, J. A. Sustainable hydrogen production. *Science* **2004**, *305*, 972.

(2) Walter, M. G.; Warren, E. L.; McKone, J. R.; Boettcher, S. W.; Mi, Q.; Santori, E. A.; Lewis, N. S. Solar water splitting cells. *Chem. Rev.* **2010**, *110*, 6446−6473.

(3) Kubacka, A.; Garcia, M. F.; Colon, G. Advanced nanoarchitectures for solar photocatalytic applications. *Chem. Rev.* **2012**, *112*, 1555−1614.

(4) Jiao, Y.; Zheng, Y.; Jaroniec, M.; Qiao, S. Z. Design of electrocatalysts for oxygen- and hydrogen-involving energy conversion reactions. *Chem. Soc. Rev.* **2015**, *44*, 2060−2086.

(5) Zou, X.; Zhang, Y. Noble metal-free hydrogen evolution catalysts for water splitting. *Chem. Soc. Rev.* **2015**, *44*, 5148−5180.

(6) Cobo, S.; Heidkamp, J.; Jacques, P. A.; Fize, J.; Fourmond, V.; Guetaz, L.;

Jousselme, B.; Ivanova, V.; Dau, H.; Palacin, S.; Fontecave, M.; Artero, V. A Janus cobalt-based catalytic material for electro-splitting of water. *Nat. Mater.* **2012**, *11*, 802−807.

(7) Kanan, M. W.; Nocera, D. G. In situ formation of an oxygen-evolving catalyst in neutral water containing phosphate and Co^{2+}. *Science* **2008**, *321*, 1072−1075.

(8) Yuan, C. Z.; Sun, Z. T.; Jiang, Y. F.; Yang, Z. K.; Jiang, N.; Zhao, Z. W.; Qazi, U. Y.; Zhang, W. H.; Xu, A. W. One-step in situ growth of iron-nickel sulfide nanosheets on FeNi alloy foils: high-performance and self-supported electrodes for water oxidation. *Small* **2017**, *13*, 1604161.

(9) Hutchings, G. S.; Zhang, Y.; Li, J.; Yonemoto, B. T.; Zhou, X. G.; Zhu, K. K.; Jiao, F. In Situ Formation of Cobalt Oxide Nanocubanes as Efficient Oxygen Evolution Catalysts. *J. Am. Chem. Soc.* **2015**, *137*, 4223−4229.

(10) Gao, M. R.; Sheng, W. C.; Zhuang, Z. B.; Fang, Q. R.; Gu, S.; Jiang, J.; Yan, Y. S. Efficient water oxidation using nanostructured α-nickel-hydroxide as an electrocatalyst. *J. Am. Chem. Soc.* **2014**, *136*, 7077−7084.

(11) Robinson, D. M.; Go, Y. B.; Greenblatt, M.; Dismukes, G. C. Water Oxidation by λ-MnO_2: Catalysis by the Cubical Mn_4O_4 Subcluster Obtained by Delithiation of Spinel $LiMn_2O_4$. *J. Am. Chem. Soc.* **2010**, *132*, 11467−11469.

(12) McCrory, C. C.; Jung, S.; Peters, J. C.; Jaramillo, T. F. Benchmarking heterogeneous electrocatalysts for the oxygen evolution reaction. *J. Am. Chem. Soc.* **2013**, *135*, 16977−16987.

(13) Li, Y.; Wang, J.; Tian, X. K.; Ma, L. L.; Dai, C.; Yang, C.; Zhou, Z. X. Carbon doped molybdenum disulfide nanosheets stabilized on graphene for the hydrogen evolution reaction with high electrocatalytic ability. *Nanoscale* **2016**, *8*, 1676−1683.

(14) Voiry, D.; Salehi, M.; Silva, R.; Fujita, T.; Chen, M. W.; Asefa, T.; Shenoy, V.; Eda, G.; Chhowalla, M. Conducting MoS2 Nanosheets as Catalysts for Hydrogen Evolution Reaction. *Nano Lett.* **2013**, *13*, 6222−6227.

(15) Ma, R. G.; Zhou, Y.; Chen, Y. F.; Li, P. X.; Liu, Q.; Wang, J. C. Ultrafine molybdenum carbide nanoparticles composited with carbon as a highly active hydrogen‐evolution electrocatalyst. *Angew. Chem., Int. Ed.* **2015**, *54*, 14723−14727.

(16) Tian, J. Q.; Cheng, N. Y.; Liu, Q.; Xing, W.; Sun, X. P. Cobalt phosphide nanowires: efficient nanostructures for fluorescence sensing of biomolecules and photocatalytic evolution of dihydrogen from water under visible light. *Angew. Chem., Int. Ed.* **2015**, *127*, 5583–5587.

(17) Zhu, W. X.; Tang, C.; Liu, D. N.; Wang, J. L.; Asiric, A. M.; Sun, X. P. A self-standing nanoporous MoP_2 nanosheet array: an advanced pH-universal catalytic electrode for the hydrogen evolution reaction. *J. Mater. Chem. A* **2016**, *4*, 7169−7173.

(18) Kibsgaard, J.; Tsai, C.; Chan, K.; Benck, J. D.; Nørskov, J. K.; Abild-Pedersen, F.; Jaramillo, T. F. Designing an improved transition metal phosphide catalyst for hydrogen evolution using experimental and theoretical trends. *Energy Environ. Sci.* **2015**, *8*, 3022−3029.

(19) Cook, T. R.; Dogutan, D. K.; Reece, S. Y.; Surendranath, Y.; Teets, T. S.; Nocera, D. G. Solar energy supply and storage for the legacy and nonlegacy worlds. *Chem. Rev.* **2010**, *110*, 6474−6502.

(20) Matsumoto, Y.; Sato, E. Electrocatalytic properties of transition metal oxides for oxygen evolution reaction. *Mater. Chem. Phys.* **1986**, *14*, 397−426.

(21) Bockris, J. O. M. Kinetics of activation controlled consecutive electrochemical reactions: anodic evolution of oxygen. *J. Chem. Phys.* **1956**, *24*, 817−827.

(22) Krasil'shchkov, A. I. Intermediate stages of oxygen anodic evolution. *Zh. Fiz. Khim.* **1963**, *37*, 273.

(23) Wade, W. H.; Hackerman, N. Anodic phenomena at an iron electrode. *Trans. Faraday Soc.* **1957**, *53*, 1636−1647.

(24) O'Grady, W. E.; Iwakura, C.; Huang, J.; Yeager, E. *The Electrochemical Society*,

ed. M. W. Breiter, Princeton **1974**, p. 286.

(25) O'Grady, W. E.; Iwakura, C.; Yeager, E. *American Society of Mechanical Engineers* **1976**, 76-ENAs-37.

(26) Aikens, D. A. *J. Chem. Educ.* **1983**, *60*, 1, A25.

(27) Man, I. C.; Su, H.-Y.; Calle-Vallejo, F.; Hansen, H. A.; Martínez, J. I.; Inoglu, N. G.; Kitchin, J.; Jaramillo, T. F.; Nørskov, J. K.; Rossmeisl, J. Universality in oxygen evolution electrocatalysis on oxide surfaces. *ChemCatChem* **2011**, *3*, 1159−1165.

(28) Faber M. S.; Jin, S. Earth-abundant inorganic electrocatalysts and their nanostructures for energy conversion applications. *Energy Environ. Sci.*, **2014**, *7*, 3519−3542.

(29) Burstein, G. A hundred years of Tafel's Equation: 1905-2005. *Corros. Sci.* **2005**, *47*, 2858−2870.

(30) Fabbri, E.; Habereder, A.; Waltar, K.; Kötz, R.; Schmidt, T. J. Developments and perspectives of oxide-based catalysts for the oxygen evolution reaction. *Catal. Sci. Technol.* **2014**, *4*, 3800−3821.

(31) Anantharaj, S.; Karthik, P. E.; Subramanian, B.; Kundu, S. Pt nanoparticle anchored molecular self-assemblies of DNA: an extremely stable and efficient HER electrocatalyst with ultralow Pt content. *ACS Catal.* **2016**, *6*, 4660−4672.

(32) Anantharaj, S.; Jayachandran, M.; Kundu, S. Unprotected and interconnected Ru^0 nano-chain networks: advantages of unprotected surfaces in catalysis and electrocatalysis. *Chem. Sci.* **2016**, *7*, 3188−3205.

(33) Kumar, T. N.; Sivabalan, S.; Chandrasekaran, N.; Phani, K. L. Synergism between polyurethane and polydopamine in the synthesis of Ni–Fe alloy monoliths. *Chem. Commun.* **2015**, *51*, 1922−1925.

(34) Yoon, Y.; Yan, B.; Surendranath, Y. Suppressing ion transfer enables versatile measurements of electrochemical surface area for intrinsic activity comparisons. *J. Am.*

Chem. Soc. **2018**, *140*, 2397−2400.

(35) Shi, Y.; Zhang, B. Recent advances in transition metal phosphide nanomaterials: synthesis and applications in hydrogen evolution reaction. *Chem. Soc. Rev.* **2016**, *45*, 1529−1541.

(36) Guo, S.; Liu, Y.; Bond, A. M.; Zhang, J.; Karthik, P. E.; Maheshwaran, I.; Kumar, S. S.; Phani, K. L. N. Facile electrochemical co-deposition of a graphene–cobalt nanocomposite for highly efficient water oxidation in alkaline media: direct detection of underlying electron transfer reactions under catalytic turnover conditions. *Phys. Chem. Chem. Phys.* **2014**, *16*, 19035−19045.

(37) Görlin, M.; Chernev, P.; Araújo, J. F.; Reier, T.; Dresp, S.; Paul, B.; Krähnert, R.; Dau, H.; Strasser, P. Oxygen Evolution Reaction Dynamics, Faradaic Charge Efficiency, and the Active Metal Redox States of Ni−Fe Oxide Water Splitting Electrocatalysts. *J. Am. Chem. Soc.* **2016**, *138*, 5603−5614.

(38) Comotti, M.; Li, W.-C.; Spliethoff, B.; Schüth, F. Support effect in high activity gold catalysts for CO oxidation. *J. Am. Chem. Soc.* **2006**, *128*, 917–924.

(39) Ng, J. W. D.; García-Melchor, M.; Bajdich, M.; Chakthranont, P.; Kirk, C.; Vojvodic, A.; Jaramillo, T. F. Gold-supported cerium-doped NiOx catalysts for water oxidation. *Nat. Energy* **2016**, *1*, 16053.

(40) Shi, Z. P.; Wang, X.; Ge, J. J.; Liu, C. P.; Xing, W. Fundamental understanding of the acidic oxygen evolution reaction: mechanism study and state-of-the-art catalysts. *Nanoscale* **2020**, *12*, 13249−13275.

(41) Yin, H.; Hui, K. S.; Zhao, X.; Mei, S.; Lv, X.; Hui, K. N. J. Chen, Eco-Friendly Synthesis of Self-Supported N-Doped Sb2S3-Carbon Fibers with High Atom Utilization and Zero Discharge for Commercial Full Lithium-Ion Batteries. *ACS Appl. Energy Mater.* **2020**, *3*, 6897.

(42) Yu, X. X.; Wang, L.; Yin, H. Hierarchical heterojunction structures based-on layered Sb_2Te_3 nanoplate@rGO for extended long-term life and high-rate capability of

sodium batteries. *Appl. Mater. Today* **2019**, *5*, 582.

(43) Huang, L. B.; Zhao, L.; Zhang, Y.; Chen, Y. Y.; Zhang, Q. H.; Luo, H.; Zhang, X.; Tang, T.; Gu, L.; Hu, J. S. Hydrogen Evolution: Self‐Limited on‐Site Conversion of MoO_3 Nanodots into Vertically Aligned Ultrasmall Monolayer MoS_2 for Efficient Hydrogen Evolution. *Adv. Energy Mater.* **2018**, *8*, 1800734.

(44) Li, J.-S.; Wang, Y.; Liu, C.-H.; Li, S.-L.; Wang, Y.-G.; Dong, L.-Z.; Dai, Z.-H.; Li, Y.-F.; Lan, Y.-Q. Coupled molybdenum carbide and reduced graphene oxide electrocatalysts for efficient hydrogen evolution. *Nat. Commun.* **2016**, *7*, 11204.

(45) Han, W. W.; Chen, L. L.; Ma, B.; Wang, J.; Song, W. Y.; Fan, X. B.; Li, Y.; Zhang, F. B.; Peng, W. C. Ultra-small Mo_2C nanodots encapsulated in nitrogen-doped porous carbon for pH-universal hydrogen evolution: insights into the synergistic enhancement of HER activity by nitrogen doping and structural defects. *J. Mater. Chem. A* **2019**, *7*, 4734−4743.

(46) Yang, Y.; Lin, Z. Y.; Gao, S. Q.; Su, J. W.; Lun, Z. Y.; Xia, G. L.; Chen, J. T.; Zhang, R. R.; Chen, Q. W. Tuning electronic structures of nonprecious ternary alloys encapsulated in graphene layers for optimizing overall water splitting activity. *ACS Catal.* **2017**, *7*, 469−479.

(47) Su, J.; Yang, Y.; Xia, G.; Chen, J.; Jiang, P.; Chen, Q. Ruthenium-cobalt nanoalloys encapsulated in nitrogen-doped graphene as active electrocatalysts for producing hydrogen in alkaline media. *Nat. Commun.* **2017**, *8*, 14969.

(48) Gao, M. R.; Cao, X.; Gao, Q.; Xu, Y. F.; Zheng, Y. R.; Jiang, J.; Yu, S. H. Nitrogen-Doped Graphene Supported $CoSe_2$ Nanobelt Composite Catalyst for Efficient Water Oxidation. *ACS Nano* **2014**, *8*, 3970−3978.

(49) Li, W. J.; Shen, Q.; Men, D. D.; Sun, Y. J.; Cao, W. W.; Lee, J. Y.; Kang, B. T.; Sun, Y. Q.; Li, C. C. Porous $CoSe_2$@N-Doped Carbon Nanowires: An Ultra-High Stable and Large-Current-Density Oxygen Evolution Electrocatalysts. *Chem. Commun.* **2021**, DOI: 10.1039/D0CC07647C.

(50) Yuan, C. Z.; Jiang, Y. F.; Wang, Z.; Xie, X.; Yang, Z. K.; Yousaf, A. B.; Xu, A. W. Cobalt phosphate nanoparticles decorated with nitrogen-doped carbon layers as highly active and stable electrocatalysts for the oxygen evolution reaction. *J. Mater. Chem. A* **2016**, *4*, 8155−8160.

(51) Li, F.; Du, J.; Li, X. N.; Shen, J. Y.; Wang, Y.; Zhu, Y.; Sun, L. C. Integration of FeOOH and Zeolitic Imidazolate Framework‐Derived Nanoporous Carbon as an Efficient Electrocatalyst for Water Oxidation. *Adv. Energy Mater.* **2018**, *8*, 1702598.

(52) Wang, H.; Zhu, Q.-L.; Zou, R.; Xu, Q. Metal-organic frameworks for energy applications. *Chem* **2017**, *2*, 52.

(53) Hu, E. L.; Ning, J. Q.; He, B.; Li, Z. P.; Zheng, C. C.; Zhong, Y. J.; Zhang, Z. Y.; Hu, Y. Unusual formation of tetragonal microstructures from nitrogen-doped carbon nanocapsules with cobalt nanocores as a bi-functional oxygen electrocatalyst. *J. Mater. Chem. A* **2017**, *5*, 2271−2279.

(54) Tavakkoli, M.; Holmberg, N.; Kronberg, R.; Jiang, H.; Sainio, J.; Kauppinen, E. I.; Kallio, T.; Laasonen, K. Electrochemical Activation of Single-Walled Carbon Nanotubes with Pseudo-Atomic-Scale Platinum for the Hydrogen Evolution Reaction. *ACS Catal.* **2017**, *7*, 3121−3130.

(55) Jiang, P.; Chen, J.; Wang, C.; Yang, K.; Gong, S.; Liu, S.; Lin, Z.; Li, M.; Xia, G.; Yang, Y.; Su, J.; Chen, Q. Tuning the Activity of Carbon for Electrocatalytic Hydrogen Evolution via an Iridium‐Cobalt Alloy Core Encapsulated in Nitrogen‐Doped Carbon Cages. *Adv. Mater.* **2018**, *30*, 1705324.

(56) Tavakkoli, M.; Kallio, T.; Reynaud, O.; Nasibulin, A. G.; Johans, C.; Sainio, J.; Jiang, H.; Kauppinen, E. I.; Laasonen, K. Single-Shell Carbon-Encapsulated Iron Nanoparticles: Synthesis and High Electrocatalytic Activity for Hydrogen Evolution Reaction. *Angew. Chem., Int. Ed.* **2015**, *54*, 4535−4538.

(57) Zhang, J.; Zhang, Q. Y.; Feng, X. L. Support and interface effects in water‐splitting electrocatalysts. *Adv. Mater.* **2019**, *31*, 1808167.

(58) Dang, S.; Zhu, Q.-L.; Xu, Q. Nanomaterials derived from metal–organic frameworks. *Nat. Rev. Chem.* **2018**, *3*, 17075.

(59) Tavakkoli, M.; Nosek, M.; Sainio, J.; Davodi, F.; Kallio, T.; Joensuu, P. M.; Laasonen, K. Functionalized Carbon Nanotubes with Ni(II) Bipyridine Complexes as Efficient Catalysts for the Alkaline Oxygen Evolution Reaction. *ACS Catal.* **2017**, *7*, 8033−8041.

(60) Zhang, H.; Ma, Z.; Duan, J.; Liu, H.; Liu, G.; Wang, T.; Chang, K.; Li, M.; Shi, L.; Meng, X.; Wu, K.; Ye, J. Active sites implanted carbon cages in core–shell architecture: highly active and durable electrocatalyst for hydrogen evolution reaction. *ACS Nano* **2016**, *10*, 684.

(61) Tsai, C.; Abild-Pedersen, F.; Nørskov, J. K. Tuning the MoS2 Edge-Site Activity for Hydrogen Evolution via Support Interactions. *Nano Lett.* **2014**, *14*, 1381.

(62) Hellstern, T. R.; Kibsgaard, J.; Tsai, C.; Palm, D. W.; King, L. A.; Abild-Pedersen, F.; Jaramillo, T. F. Investigating Catalyst–Support Interactions To Improve the Hydrogen Evolution Reaction Activity of Thiomolybdate $[Mo_3S_{13}]^{2-}$ Nanoclusters. *ACS Catal.* **2017**, *7*, 7126.

(63) Yeo, B. S.; Bell, A. T. Enhanced activity of gold-supported cobalt oxide for the electrochemical evolution of oxygen. *J. Am. Chem. Soc.* **2011**, *133*, 5587–5593.

(64) Yuan, C. Z.; Zhong, S. L.; Jiang, Y. F.; Yang, Z. K.; Zhao, Z. W.; Zhao, S. J.; Jiang, N.; Xu, A. W. Direct growth of cobalt-rich cobalt phosphide catalysts on cobalt foil: an efficient and self-supported bifunctional electrode for overall water splitting in alkaline media. *J. Mater. Chem. A* **2017**, *5*, 10561−10566.

(65) Chen, S.; Qiao, S. Z. Hierarchically Porous Nitrogen-Doped Graphene-$NiCo_2O_4$ Hybrid Paper as an Advanced Electrocatalytic Water-Splitting Material. *ACS Nano* **2013**, *7*, 10190−10196.

(66) Chen, S.; Duan, J.; Ran, J.; Jaroniec, M.; Qiao, S. Z. N-doped Graphene Film-Confined Nickel Nanoparticles as a Highly Efficient Three-Dimensional Oxygen

Evolution Electrocatalyst. *Energy Environ. Sci.* **2013**, *6*, 3693−3699.

(67) Liang, Y.; Li, Y.; Wang, H.; Zhou, J.; Wang, J.; Regier, T.; Dai, H. Co_3O_4 Nanocrystals on Graphene as a Synergistic Catalyst for Oxygen Reduction Reaction. *Nat. Mater.* **2011**, *10*, 780−786.

(68) Chen, S.; Duan, J.; Jaroniec, M.; Qiao, S. Z. Three-Dimensional N-Doped Graphene Hydrogel/NiCo Double Hydroxide Electrocatalysts for Highly Efficient Oxygen Evolution. *Angew. Chem., Int. Ed.* **2013**, *52*, 13567−13570.

(69) Ma, T. Y.; Dai, S.; Jaroniec, M.; Qiao, S. Z. Graphitic Carbon Nitride Nanosheet−Carbon Nanotube Three Dimensional Porous Composites as High-Performance Oxygen Evolution Electrocatalysts. *Angew. Chem., Int. Ed.* **2014**, *53*, 7281−7285.

(70) Yuan, C. Z.; Jiang, Y. F.; Zhao, Z. W.; Zhao, S. J.; Zhou, X.; Cheang, T. Y.; Xu, A. W. Molecule-Assisted Synthesis of Highly Dispersed Ultrasmall RuO_2 Nanoparticles on Nitrogen-Doped Carbon Matrix as Ultraefficient Bifunctional Electrocatalysts for Overall Water Splitting. *ACS Sustainable Chem. Eng.* **2018**, *6*, 11529−11535.

(71) Wang, J.; Cui, W.; Liu, Q.; Xing, Z.; Asiri, A. M.; Sun, X. Recent progress in cobalt-based heterogeneous catalysts for electrochemical water splitting. *Adv. Mater.* **2016**, *28*, 215.

(72) Zhu, Y. P.; Guo, C.; Zheng, Y.; Qiao, S. Z. Surface and interface engineering of noble-metal-free electrocatalysts for efficient energy conversion processes. *Acc. Chem. Res.* **2017**, *50*, 915.

(73) Hunter, B. M.; Blakemore, J. D.; Deimund, M.; Gray, H. B.; Winkler, J. R.; Muller, A. M. Highly Active Mixed-Metal Nanosheet Water Oxidation Catalysts Made by Pulsed-Laser Ablation in Liquids. *J. Am. Chem. Soc.* **2014**, *136*, 13118−13121.

(74) Subbaraman, R.; Tripkovic, D.; Chang, K.-C.; Strmcnik, D.; Paulikas, A. P.; Hirunsit, P.; Chan, M.; Greeley, J.; Stamenkovic, V.; Markovic, N. M. Trends in activity for the water electrolyser reactions on 3d M(Ni, Co, Fe, Mn) hydr(oxy)oxide catalysts.

Nat. Mater. **2012**, *11*, 550.

(75) Subbaraman, R.; Tripkovic, D.; Strmcnik, D.; Chang, K.-C.; Uchimura, M.; Paulikas, A. P.; Stamenkovic, V.; Markovic, N. M. Enhancing hydrogen evolution activity in water splitting by tailoring Li^+-$Ni(OH)_2$-Pt interfaces. *Science* **2011**, *334*, 1256.

(76) Song, F. Z.; Li, W.; Yang, J. Q.; Han, G. Q.; Liao, P. L.; Sun, Y. J. Interfacing nickel nitride and nickel boosts both electrocatalytic hydrogen evolution and oxidation reactions. *Nat. Commun.* **2018**, *9*, 4531.

(77) Yu, Q. M.; Luo, Y. T.; Qiu, S. Y.; Li, Q. Y.; Cai, Z. Y.; Zhang, Z. Y.; Liu, J. M.; Sun, C. H.; Liu, B. L. Tuning the hydrogen evolution performance of metallic 2D tantalum disulfide by interfacial engineering. *ACS Nano* **2019**, *13*, 11874−11881.

(78) Wang, F. M.; He, P.; Li, Y. C.; Shifa, T. A.; Deng, Y.; Liu, K. L.; Wang, Q. S.; Wang, F. ; Wen, Y.; Wang, Z. X.; Zhan, X. Y.; Sun, L. F.; He, J. Interface Engineered W_xC@WS_2 Nanostructure for Enhanced Hydrogen Evolution Catalysis. *Adv. Funct. Mater.* **2017**, *27*, 1605802.

(79) Diao, J. X.; Qiu, Y.; Liu, S. Q.; Wang, W. T.; Chen, K.; Li, H. L.; Yuan, W. Y.; Qu, Y. T.; Guo, X. H. Interfacial Engineering of W_2N/WC Heterostructures Derived from Solid-State Synthesis: A Highly Efficient Trifunctional Electrocatalyst for ORR, OER, and HER. *Adv. Mater.* **2020**, *32*, 1905679.

(80) Gao, M. R.; Xu, Y. F.; Jiang, J.; Zheng, Y. R.; Yu, S. H. Water Oxidation Electrocatalyzed by an Efficient Mn_3O_4/$CoSe_2$ Nanocomposite. *J. Am. Chem. Soc.* **2012**, *134*, 2930−2933.

(81) Zhang, Z.; Ma, X. X.; Tang, J. L. Porous $NiMoO_{4-x}$/MoO_2 hybrids as highly effective electrocatalysts for the water splitting reaction. *J. Mater. Chem. A* **2018**, *6*, 12361−12369.

(82) Han, J. C.; Wang, R.; Zhang, Y. Y.; Wang, X. J.; Zhang, X. H.; Zhang, Z. H.; Zhang, Y. M.; Song, B.; Jin, S. Improving Electrocatalysts for Oxygen Evolution Using Ni_xFe_{3-}

$_xO_4$/Ni Hybrid Nanostructures Formed by Solvothermal Synthesis. *ACS Energy Lett.* **2018**, *3*, 1698−1707.

(83) Yin, J.; Li, Y. X.; Lv, F.; Lu, M.; Sun, K.; Wang, W.; Wang, L.; Cheng, F. Y.; Li, Y. F.; Xi, P. X.; Guo, S. J. Oxygen Vacancies Dominated NiS_2/CoS_2 Interface Porous Nanowires for Portable Zn–Air Batteries Driven Water Splitting Devices. *Adv. Mater*. **2017**, *29*, 1704681.

(84) Xu, J. Y.; We, X. K.; Costa, J. O.; Lado, J. L.; Owens-Baird, B.; Gonçalves, L. P. L.; Fernandes, S. P. S.; Heggen, M.; Petrovykh, D. Y.; Dunin-Borkowski. R. E.; Kovnir, K.; Koleńko, Y. V. Interface engineering in nanostructured nickel phosphide catalyst for efficient and stable water oxidation. *ACS Catal.* **2017**, *7*, 5450−5455.

(85) Zhang, J.; Wang, T.; Pohl, D.; Rellinghaus, B.; Dong, R.; Liu, S.; Zhuang, X.; Feng, X. Interface Engineering of MoS_2/Ni_3S_2 Heterostructures for Highly Enhanced Electrochemical Overall-Water-Splitting Activity. *Angew. Chem., Int. Ed.* **2016**, *55*, 6702−6707.

(86) Yu, D. H.; Ye, M.; Han, S. L.; Ma, Y. C.; Hu, F.; Li, L. L.; Peng, S. J. Hierarchical Fe_3C-Mo_2C-Carbon Hybrid Electrocatalysts Promoted through a Strong Charge-Transfer Effect. *ChemSusChem* **2020**, *13*, 5280−5287.

(87) Li, Y. B.; Tan, X.; Tan, H.; Ren, H. J.; Chen, S.; Yang, W. F.; Smith, S. C.; Zhao, C. Phosphine vapor-assisted construction of heterostructured $Ni_2P/NiTe_2$ catalysts for efficient hydrogen evolution. *Energy Environ. Sci.* **2020**, *13*, 1799−1807.

(88) Gong, M.; Zhou, W.; Tsai, M.-C.; Zhou, J.; Guan, M.; Lin, M.-C.; Zhang, B.; Hu, Y.; Wang, D.-Y.; Yang, J.; Pennycook, S. J.; Hwang, B.-J.; Dai, H. Nanoscale nickel oxide/nickel heterostructures for active hydrogen evolution electrocatalysis. *Nat. Commun.* **2014**, *5*, 4695.

(89) Sun, L. M.; Zhan, W. W.; Li, Y. A.; Wang, F.; Zhang X. L.; Han, X, G. Understanding the facet-dependent catalytic performance of hematite microcrystals in a CO oxidation reaction. *Inorg. Chem. Front.* **2018**, *5*, 2332−2339.

(90) Chen, Z.; Kronawitter C. X.; Koe, B. E. Facet-dependent activity and stability of Co_3O_4 nanocrystals towards the oxygen evolution reaction. *Phys. Chem. Chem. Phys.* **2015**, *17*, 29387−29393.

(91) Yang, H. D.; Luo, S.; Li, X. Z.; Li, S. W.; Jin J.; Ma, J. T. Controllable orientation-dependent crystal growth of high-index faceted dendritic $NiC_{0.2}$ nanosheets as high-performance bifunctional electrocatalysts for overall water splitting. *J. Mater. Chem. A* **2016**, *4*, 18499−18508.

(92) Gloag, L.; Benedetti, T. M.; Cheong, S.; Marjo, C. E.; Gooding, J. J.; Tilley, R. D. Cubic-core hexagonal-branch mechanism to synthesize bimetallic branched and faceted Pd–Ru nanoparticles for oxygen evolution reaction electrocatalysis. *J. Am. Chem. Soc.* **2018**, *140*, 12760−12764.

(93) Li, C. J.; Luo, M. C.; Xia, Z. H.; Guo, S. J. High-index faceted noble metal nanostructures drive renewable energy electrocatalysis. *Nano Materials Science* **2020**, *2*, 309−315.

(94) Poerwoprajitno, A. R.; Gloag, L.; Benedetti, T. M.; Cheong, S.; Watt, J.; Huber, D. L.; Gooding, J. J.; Tilley, R. D. Formation of branched ruthenium nanoparticles for improved electrocatalysis of oxygen evolution reaction. *Small* **2019**, *15*, 1804577.

(95) Markovića, N. M.; Sarraf, S. T.; Gasteiger, H. A.; Ross, P. N. Hydrogen electrochemistry on platinum low-index single-crystal surfaces in alkaline solution. *J. Chem. Soc., Faraday Trans.* **1996**, *92*, 3719−3725.

(96) Marković, N. M.; Grgur, B. N.; Ross, P. N. Temperature-dependent hydrogen electrochemistry on platinum low-index single-crystal surfaces in acid solutions. *J. Phys. Chem. B* **1997**, *101*, 5405−5413.

(97) Chang, S. H.; Danilovic, N.; Chang, K.-C.; Subbaraman, R.; Paulikas, A. P.; Fong, D. D.; Highland, M. J.; Baldo, P. M.; Stamenkovic, V. R.; Freeland, J. W.; Eastman, J. A.; Markovic, N. M. Functional links between stability and reactivity of strontium ruthenate single crystals during oxygen evolution. *Nat. Commun.* **2014**, *5*, 4191.

(98) Bolar, S.; Shit, S.; Murmu, N. C.; Samanta, P.; Kuila, T. Activation Strategy of MoS_2 as HER Electrocatalyst through Doping-Induced Lattice Strain, Band Gap Engineering, and Active Crystal Plane Design. *ACS Appl. Mater. Interfaces* **2021**, *13*, 765−780.

(99) Luo, Q. X.; Lin, D.; Zhan, W. Q.; Zhang, W. Q.; Tang, L. L.; Luo, J. J.; Gao, Z.; Jiang, P.; Wang, M.; Hao, L. Y.; Tang, K. B. Hexagonal Perovskite $Ba_{0.9}Sr_{0.1}Co_{0.8}Fe_{0.1}Ir_{0.1}O_{3-\delta}$ as an Efficient Electrocatalyst towards the Oxygen Evolution Reaction. *ACS Appl. Energy Mater.* **2020**, *3*, 7149−7158.

(100) Hao, X.; Yoko, A.; Chen, C.; Inoue, K.; Saito, M.; Seong, G.; Takami, S.; Adschiri, T.; Ikuhara, Y. Atomic-Scale Valence State Distribution inside Ultrafine CeO_2 Nanocubes and Its Size Dependence. *Small* **2018**, *14*, 1802915.

(101) Zhu, C. R.; Wang, A. L.; Xiao, W.; Chao, D. L.; Zhang, X.; Tiep, N. H.; Chen, S.; Kang, J. N.; Wang, X.; Ding, J.; Wang, J.; Zhang, H.; Fan, H. J. In Situ Grown Epitaxial Heterojunction Exhibits High-Performance Electrocatalytic Water Splitting. *Adv. Mater.* **2018**, *30*, 1705516.

(102) Han, X. P.; He, G. W.; He, Y.; Zhang, J. F.; Zheng, X. R.; Li, L. L.; Zhong, C.; Hu, W. B.; Deng, Y. D.; Ma, T. Y. Metal Air Batteries: Engineering Catalytic Active Sites on Cobalt Oxide Surface for Enhanced Oxygen Electrocatalysis. *Adv. Energy Mater.* **2018**, *8*, 1702222.

(103) Wei, R. J.; Fang, M.; Dong, G. F.; Lan, C. Y.; Shu, L.; Zhang, H.; Bu, X. M.; Ho, J. C. High-Index Faceted Porous Co_3O_4 Nanosheets with Oxygen Vacancies for Highly Efficient Water Oxidation. *ACS Appl. Mater. Interfaces* **2018**, *10*, 7079.

(104) Feng, L. L.; Yu, G. T.; Wu, Y. Y.; Li, G.-D.; Li, H.; Sun, Y. H.; Asefa, T.; Chen, W.; Zou, X. X. High-Index Faceted Ni_3S_2 Nanosheet Arrays as Highly Active and Ultrastable Electrocatalysts for Water Splitting. *J. Am. Chem. Soc.* **2015**, *137*, 14023−14026.

(105) Kou, Z. K.; Xi, K.; Pu, Z. H.; Mu, S. C. Constructing carbon-cohered high-index

(222) faceted tantalum carbide nanocrystals as a robust hydrogen evolution catalyst. *Nano Energy* **2017**, *36*, 374−380.

(106) Deng, S. J.; Zhang, K. L.; Xie, D.; Zhang, Y.; Zhang, Y. Q.; Wang, Y. D.; Wu, J. B.; Wang, X. L.; Fan, H. J.; Xia, X. H.; Tu, J. P. High-Index-Faceted Ni_3S_2 Branch Arrays as Bifunctional Electrocatalysts for Efficient Water Splitting. *Nano-Micro Lett.* **2019**, *11*, 12.

(107) Liu, Y. D.; Dinh, K. N.; Dai, Z. F.; Yan, Q. Y. Metallenes: Recent Advances and Opportunities in Energy Storage and Conversion Applications. *ACS Materials Lett.* **2020**, *2*, 1148−1172.

(108) Poerwoprajitno, A. R.; Gloag, L.; Cheong, S.; Gooding, J. J.; Tilley, R. D. Synthesis of low-and high-index faceted metal (Pt, Pd, Ru, Ir, Rh) nanoparticles for improved activity and stability in electrocatalysis. *Nanoscale* **2019**, *11*, 18995−19011.

(109) Xie, S. F.; Choi, S.; Xia, X. B.; Xia, Y. N. Catalysis on faceted noble-metal nanocrystals: both shape and size matter. *Curr. Opin. Chem. Eng.* **2013**, *2*, 142−150.

(110) Fan, Z.; Huang, X.; Han, Y.; Bosman, M.; Wang, Q.; Zhu, Y.; Liu, Q.; Li, B.; Zeng, Z.; Wu, J.; Shi, W.; Li, S.; Gan, C. L.; Zhang, H. Surface Modification-Induced Phase Transformation of Hexagonal Close-Packed Gold Square Sheets. *Nat. Commun.* **2015**, *6*, 6571.

(111) Zhao, M.; Figueroa-Cosme, L.; Elnabawy, A. O.; Vara, M.; Yang, X.; Roling, L. T.; Chi, M.; Mavrikakis, M.; Xia, Y. Synthesis and Characterization of Ru Cubic Nanocages with a Face-Centered Cubic Structure by Templating with Pd Nanocubes. *Nano Lett.* **2016**, *16*, 5310−5317.

(112) Fan, F. R.; Liu, D. Y.; Wu, Y. F.; Duan, S.; Xie, Z. X.; Jiang, Z. Y.; Tian, Z. Q. Epitaxial Growth of Heterogeneous Metal Nanocrystals: from Gold Nano-octahedra to Palladium and Silver Nanocubes. *J. Am. Chem. Soc.* **2008**, *130*, 6949−6951.

(113) Balogun, M. S.; Qiu, W. T.; Huang, Y. C.; Yang, H.; Xu, R. M.; Zhao, W. X.; Li, G. R.; Ji, H. B.; Tong. Y. X. Cost-Effective Alkaline Water Electrolysis Based on

Nitrogen-and Phosphorus-Doped Self-Supportive Electrocatalysts. *Adv. Mater.* **2017**, *29*, 1702095.

(114) Wang, J. M.; Ma, X.; Qu, F. L.; Asiri, A. M.; Sun, X. P. Fe-Doped Ni_2P Nanosheet Array for High-Efficiency Electrochemical Water Oxidation. *Inorg. Chem.* **2017**, *56*, 1041−1044.

(115) Sultana, U. K.; Riches, J. D.; O'Mullane, A. P. Gold Doping in a Layered Co-Ni Hydroxide System via Galvanic Replacement for Overall Electrochemical Water Splitting. *Adv. Funct. Mater.* **2018**, *28*, 1804361.

(116) Zhang, G.; Feng, Y. S.; Lu, W. T.; He, D.; Wang, C. Y.; Li, Y. K.; Wang, K. Y.; Cao, F. F. Enhanced Catalysis of Electrochemical Overall Water Splitting in Alkaline Media by Fe Doping in Ni_3S_2 Nanosheet Arrays. *ACS Catal.* **2018**, *8*, 5431−5441.

(117) Li, Y. G.; Hasin, P.; Wu, Y. Y. $Ni_xCo_{3-x}O_4$ Nanowire Arrays for Electrocatalytic Oxygen Evolution. *Adv. Mater.* **2010**, *22*, 1926−1929.

(118) Zhou, Q. W.; Shen, Z. H.; Zhu, C.; Li, J. C.; Ding, Z. Y.; Wang, P.; Pan, F.; Zhang, Z. Y.; Ma, H. X.; Wang, S. Y.; Zhang, H. G. Nitrogen-Doped CoP Electrocatalysts for Coupled Hydrogen Evolution and Sulfur Generation with Low Energy Consumption. *Adv. Mater.* **2018**, *30*, 1800140.

(119) Li, Q.; Wang, X. F.; Tang, K.; Wang, M. F.; Wang, C.; Yan, C. L. Electronic Modulation of Electrocatalytically Active Center of Cu_7S_4 Nanodisks by Cobalt-Doping for Highly Efficient Oxygen Evolution Reaction. *ACS Nano* **2017**, *11*, 12230−12239.

(120) Xiong, Q. Z.; Wang, Y.; Liu, P. F.; Zheng, L. R.; Wang, G. Z.; Yang, H. G.; Wong, P. K.; Zhang, H. M.; Zhao, H. J. Cobalt Covalent Doping in MoS_2 to Induce Bifunctionality of Overall Water Splitting. *Adv. Mater.* **2018**, *30*, 1801450.

(121) Alarawi, A.; Ramalingam, V.; He, J. H. Recent advances in emerging single atom confined two-dimensional materials for water splitting applications. *Mater. Today Energy*, **2019**, *11*, 1−23.

(122) Liu, W.; Zhang, H. X.; Li, C. M.; Wang, X.; Liu, J. Q.; Zhang, X. W. Non-noble metal single-atom catalysts prepared by wet chemical method and their applications in electrochemical water splitting. *Journal of Energy Chemistry* **2020**, *47*, 333−345.

(123) Zhu, C. Z.; Shi, Q. R.; Feng, S.; Du, D.; Lin, Y. H. Single-Atom Catalysts for Electrochemical Water Splitting. *ACS Energy Lett.* **2018**, *3*, 1713−1721.

(124) Zhu, J. T.; Cai, L. J.; Yin, X. M.; Wang, Z.; Zhang, L. F.; Ma, H. B.; Ke, Y. X.; Du, Y. H.; Xi, S. B.; Wee, A. T. S.; Chai, Y.; Zhang, W. J. Enhanced Electrocatalytic Hydrogen Evolution Activity in Single-Atom Pt-Decorated VS_2 Nanosheets. *ACS Nano* **2020**, *14*, 5600−5608.

(125) Luo, Z. Y.; Ouyang, Y. X.; Zhang, H.; Xiao, M. L.; Ge, J. J.; Jiang, Z.; Wang, J. L.; Tang, D. M.; Cao, X. Z.; Liu, C. P.; Xing, W. Chemically activating MoS_2 via spontaneous atomic palladium interfacial doping towards efficient hydrogen evolution. *Nat. Commun*. **2018**, *9*, 2120.

(126) Yan, J. Q.; Kong, L. Q.; Ji, Y. J.; White, J.; Li, Y. Y.; Zhang, J.; An, P. F.; Liu, S. Z.; Lee, S. T.; Ma, T. Y. Single atom tungsten doped ultrathin α-Ni (OH) 2 for enhanced electrocatalytic water oxidation. *Nat. Commun.* **2019**, *10*, 2149.

(127) Yao, N.; Li, P.; Zhou, Z. R.; Zhao, Y. M.; Cheng, G. Z.; Chen, S. L.; Luo, W. Hydrogen Evolution Reaction: Synergistically Tuning Water and Hydrogen Binding Abilities Over Co_4N by Cr Doping for Exceptional Alkaline Hydrogen Evolution Electrocatalysis. *Adv. Energy Mater.* **2019**, *9*, 1902449.

(128) Chen, Q. Q.; Hou, C. C.; Wang, C. J.; Yang, X.; Shi, R.; Chen, Y. Ir^{4+}-Doped NiFe LDH to expedite hydrogen evolution kinetics as a Pt-like electrocatalyst for water splitting. *Chem. Commun.* **2018**, *54*, 6400−6403.

(129) Fan, H. S.; Yu, H.; Zhang, Y. F.; Zheng, Y.; Luo, Y. B.; Dai, Z. F.; Li, B.; Zong, Y.; Yan, Q. Y. F-Doped Ni_3C Nanodots in N-Doped Carbon Nanosheets for Efficient Hydrogen‐Evolution and Oxygen‐Evolution Electrocatalysis. *Angew. Chem., Int. Ed.* **2017**, *56*, 12566−12570.

(130) Han, N.; Yang, K. R.; Lu, Z. Y.; Li, Y. G.; Xu, W. W.; Gao, T. F.; Cai, Z.; Zhang, Y.; Batista, V. S.; Liu, W.; Sun, X. M. Nitrogen-doped tungsten carbide nanoarray as an efficient bifunctional electrocatalyst for water splitting in acid. *Nat. Commun.* **2018**, *9*, 924.

(131) Kang, Y.; Wang, S.; Zhu, S. Q.; Gao, H. X.; Hui, K. S.; Yuan, C. Z.; Yin, H.; Bin, F.; Wu, X. L.; Mai, W. J.; Zhu, L.; Hu, M. C.; Liang, F.; Chen, F. M.; Hui, K. N. Iron-modulated nickel cobalt phosphide embedded in carbon to boost power density of hybrid sodium–air battery. *Appl. Catal. B* **2021**, *285*, 119786.

(132) Wang, Z. C.; Liu, H. L.; Ge, R. X.; Ren, X.; Ren, J.; Yang, D. J. Zhang, L. X.; Sun, X. P. Phosphorus-Doped Co_3O_4 Nanowire Array: A Highly Efficient Bifunctional Electrocatalyst for Overall Water Splitting. *ACS Catal.* **2018**, *8*, 2236−2241.

(133) Chen, Z. Y.; Song, Y.; Cai, Zheng, X. S.; Han, D. D.; Wu, Y. S.; Zang, Y. P.; Niu, S. W.; Liu, Y.; Zhu, J. F.; Liu, X. J.; Wang, G. M. Tailoring the d-Band Centers Enables Co_4N Nanosheets To Be Highly Active for Hydrogen Evolution Catalysis. *Angew. Chem., Int. Ed.* **2018**, *57*, 5076−5080.

(134) Li, P. S.; Duan, X. X.; Kuang, Y.; Li, Y. P.; Zhang, G. X.; Liu, W.; Sun, X. M. Tuning Electronic Structure of NiFe Layered Double Hydroxides with Vanadium Doping toward High Efficient Electrocatalytic Water Oxidation. *Adv, Energy Mater.* **2018**, *8*, 1703341.

(135) Gu, C.; Hu, S. J.; Zheng, X. S.; Gao, M. R.; Zheng, Y. R.; Shi, L.; Gao, Q.; Zheng, X.; Chu, W. S.; Yao, H. B.; Zhu, J. F.; Yu, S. H. Synthesis of Sub-2 nm Iron-Doped $NiSe_2$ Nanowires and Their Surface-Confined Oxidation for Oxygen Evolution Catalysis. *Angew. Chem., Int. Ed.* **2018**, ***57***, 4020−4024.

(136) Han, H.; Choi, H.; Mhin, S.; Hong, Y.; Kim, K. M.; Kwon, J.; Ali, G.; Chung, K. Y.; Je, M.; Umh, H. N.; Lim, D.; Davey, K.; Qiao, S. Z.; Paik, U.; Song, T. Advantageous crystalline–amorphous phase boundary for enhanced electrochemical water oxidation. *Energy Environ. Sci.* **2019**, *12*, 2443−2454.

(137) Liu, Q.; Xie, L. S.; Liu, Z. A.; Du, G.; Asiri, A. M.; Sun, X. P. A Zn-doped Ni_3S_2 nanosheet array as a high-performance electrochemical water oxidation catalyst in alkaline solution. *Chem. Commun.* **2017**, *53*, 12446−12449.

(138) Wang, X. F.; Sun, P. F.; Lu, H. L.; Tang, K.; Li, Q.; Wang, C.; Mao, Z. Y.; Ali, T.; Yan, C. L. Aluminum‐Tailored Energy Level and Morphology of $Co_{3-x}Al_xO_4$ Porous Nanosheets toward Highly Efficient Electrocatalysts for Water Oxidation. *Small* **2019**, *15*, 1804886.

(139) Liang, X.; Shi, L.; Liu, Y. P.; Chen, H.; Si, R.; Yan, W. S.; Zhang, Q.; Li, G. D.; Yang, L.; Zou, X. X. Activating Inert, Nonprecious perovskites with iridium dopants for efficient oxygen evolution reaction under acidic conditions. *Angew. Chem. Int. Ed.* **2019**, *58*, 7631−7635.

(140) Hou, C. X.; Hou, Y.; Fan, Y. Q.; Zhai, Y. J.; Wang, Y.; Sun, Z. Y.; Fan, R. H.; Dang, F.; Wang, J. Oxygen vacancy derived local build-in electric field in mesoporous hollow Co_3O_4 microspheres promotes high-performance Li-ion batteries. *J. Mater. Chem. A* **2018**, *6*, 6967−6976.

(141) Ling, T.; Zhang, T.; Ge, B. H.; Han, L. L.; Zheng, L. R.; Lin, F.; Xu, Z. R.; Hu, W. B.; Du, X. W.; Davey, K.; Qiao, S. Z. Well-Dispersed Nickel-and Zinc-Tailored Electronic Structure of a Transition Metal Oxide for Highly Active Alkaline Hydrogen Evolution Reaction. *Adv. Mater.* **2019**, *31*, 1807771.

(142) An, L.; Huang, B. L.; Zhang, Y.; Wang, R.; Zhang, N.; Dai, T. Y.; Xi, P. X.; Yan, C. H. Interfacial Defect Engineering for Improved Portable Zinc–Air Batteries with a Broad Working Temperature. *Angew. Chem. Int. Ed.* **2019**, *58*, 9459−9463.

(143) Ling, T.; Yan, D. Y.; Jiao, Yan.; Wang, H.; Zheng, Y.; Zheng, X. L.; Mao, J.; Du, X. W.; Hu, Z. P.; Jaroniec, M.; Qiao, S. Z. Engineering surface atomic structure of single-crystal cobalt(II) oxide nanorods for superior electrocatalysis. *Nat. Commun.* **2016**, *7*, 12876.

(144) Liu, D. L.; Zhang, C.; Yu, Y. F.; Shi, Y. M.; Yu, Y.; Niu, Z. Q.; Zhang, Z. Hydrogen

evolution activity enhancement by tuning the oxygen vacancies in self-supported mesoporous spinel oxide nanowire arrays. *Nano Research* **2018**, *11*, 603−613.

(145) Bao, J.; Zhang, X. D.; Fan, B.; Zhang, J. J.; Zhou, M.; Yang, W. L.; Hu, X.; Wang, H.; Pan, B. C.; Xie, Y. Ultrathin spinel-structured nanosheets rich in oxygen deficiencies for enhanced electrocatalytic water oxidation. *Angew. Chem., Int. Ed.* **2015**, *54*, 7399−7404.

(146) Gao, S.; Jiao, X. C.; Sun, Z. T.; Zhang, W. H.; Sun, Y. F.; Wang, C. M.; Hu, Q. T.; Zu, X. L.; Yang, F.; Yang, S. Y. et al. Ultrathin Co_3O_4 layers realizing optimized CO_2 electroreduction to formate. *Angew. Chem., Int. Ed.* **2016**, *55*, 698−702.

(147) Zheng, T. T.; Sang, W.; He, Z. H.; Wei, Q. S.; Chen, B. W.; Li, H. L.; Cao, C.; Huang, R. J.; Yan, X. P.; Pan, B. C.; Zhou, S. M.; Zeng, J. Conductive tungsten oxide nanosheets for highly efficient hydrogen evolution. *Nano Lett.* **2017**, *17*, 7968−7973.

(148) Tian, H.; Cui, X. Z.; Zeng, L. M.; Su, L.; Song, Y. L.; Shi, J. L. Oxygen vacancy-assisted hydrogen evolution reaction of the Pt/WO_3 electrocatalyst. *J. Mater. Chem. A* **2019**, *7*, 6285−6293.

(149) Wang, Y. C.; Zhou, T.; Jiang, K.; Da, P. M.; Peng, Z.; Tang, J.; Kong, B.; Cai, W. B.; Yang, Z. Q.; Zheng, G. F. Reduced Mesoporous Co_3O_4 Nanowires as Efficient Water Oxidation Electrocatalysts and Supercapacitor Electrodes. *Adv. Energy Mater.* **2014**, *4*, 1400696.

(150) Cai, Z.; Bi, Y. M.; Hu, E. Y.; Liu, W.; Dwarica, N.; Tian, Y.; Li, X. L.; Kuang, Y.; Li, Y. P.; Yang, X. Q.; Wang, H. L.; Sun, X. M. Single‐Crystalline Ultrathin Co3O4 Nanosheets with Massive Vacancy Defects for Enhanced Electrocatalysis. *Adv. Energy Mater.* **2018**, *8*, 1701694.

(151) Xu, L.; Jiang, Q.; Xiao, Z.; Li, X.; Huo, J.; Wang, S.; Dai, L. Plasma‐Engraved Co_3O_4 Nanosheets with Oxygen Vacancies and High Surface Area for the Oxygen Evolution Reaction. *Angew. Chem., Int. Ed.* **2016**, *55*, 5277−5281.

(152) Zhang, T.; Wu, M. Y.; Yan, D. Y.; Mao, J.; Liu, H.; Hu, W. B.; Du, X. W.; Ling,

T.; Qiao, S. Z. Engineering oxygen vacancy on NiO nanorod arrays for alkaline hydrogen evolution. *Nano Energy* **2018**, *43*, 103−109.

(153) Xu, W. J.; LYu, F. L.; Bai, Y. C.; Gao, A. Q.; Feng, J.; Cai, Z. X.; Yin, Y. D. Porous cobalt oxide nanoplates enriched with oxygen vacancies for oxygen evolution reaction. *Nano Energy* **2018**, *43*, 110−116.

(154) Yang, M. Q.; Wang, J.; Wu, H.; Ho, G. W. Noble Metal-Free Nanocatalysts with Vacancies for Electrochemical Water Splitting. *Small* **2018**, *14*, 1703323.

(155) Cai, W. Z.; Yang, H. B.; Zhang, J. M.; Chen, H. C.; Tao, H. B.; Gao, J. J.; Liu, S.; Liu, W.; Li, X. N.; Liu, B. Amorphous Multimetal Alloy Oxygen Evolving Catalysts. *ACS Materials Lett.* **2020**, *2*, 624−632.

(156) Huang, G.; Xiao, Z. H.; Chen, R.; Wang, S. Y. Defect Engineering of Cobalt-Based Materials for Electrocatalytic Water Splitting. *ACS Sustainable Chem. Eng.* **2018**, *6*, 15954−15969.

(157) Zhang, W. Z.; Chen, G. Y.; Zhao, J.; Liang, J. C.; Sun, L. F.; Liu, G. F.; Ji, B. W.; Yan, X. Y.; Zhang, J. R. Self-growth Ni_2P nanosheet arrays with cationic vacancy defects as a highly efficient bifunctional electrocatalyst for overall water splitting. *J. Colloid Interface Sci.* **2020**, *561*, 638−646.

(158) Cheng, F. Y.; Shen, J.; Peng, B.; Pan, Y. D.; Tao, Z. L.; Chen, J. Rapid room-temperature synthesis of nanocrystalline spinels as oxygen reduction and evolution electrocatalysts. *Nat. Chem.* **2011**, *3*, 79−84.

(159) Kwong, W. L.; Gracia-Espino, E.; Lee, C. C.; Sandström, R.; Wågberg, T.; Messinger, J. Cationic Vacancy Defects in Iron Phosphide: A Promising Route toward Efficient and Stable Hydrogen Evolution by Electrochemical Water Splitting. *ChemSusChem* **2017**, *10*, 4544−4551.

(160) Liu, B.; Wang, Y.; Peng, H. Q.; Yang, R.; Jiang, Z.; Zhou, X. T.; Lee, C. S.; Zhao, H. J.; Zhang, W. J. Iron vacancies induced bifunctionality in ultrathin feroxyhyte nanosheets for overall water splitting. *Adv. Mater.* **2018**, *30*, 1803144.

(161) Zhang, R. R.; Zhang, Y. C.; Pan, L.; Shen, G. Q.; Mahmood, N.; Ma, Y. H.; Shi, Y.; Jia, W. Y.; Wang, L.; Zhang, X. W.; Xu, W.; Zou, J. J. Engineering cobalt defects in cobalt oxide for highly efficient electrocatalytic oxygen evolution. *ACS Catal.* **2018**, *8*, 3803−3811.

(162) Cheng, W. R.; Zhang, H.; Zhao, X.; Su, H.; Tang, F. M.; Tian, J.; Liu, Q. H. A metal-vacancy-solid-solution NiAlP nanowall array bifunctional electrocatalyst for exceptional all-pH overall water splitting. *J. Mater. Chem. A* **2018**, *6*, 9420−9427.

(163) Wang, Y. Y.; Qiao, M.; Li, Y. F.; Wang, S. Y. Tuning Surface Electronic Configuration of NiFe LDHs Nanosheets by Introducing Cation Vacancies (Fe or Ni) as Highly Efficient Electrocatalysts for Oxygen Evolution Reaction. *Small* **2018**, *14*, 1800136.

(164) Liu, Y. W.; Cheng, H.; Lyu, M. J.; Fan,S. J.; Liu, Q. H.; Zhang, W. S.; Zhi, Y. D.; Wang, C. M.; Xiao, C.; Wei, S. Q.; Ye, B. J.; Xie, Y. Low Overpotential in Vacancy-Rich Ultrathin $CoSe_2$ Nanosheets for Water Oxidation. *J. Am. Chem. Soc.* **2014**, *136*, 15670−15675.

(165) Lee, H. J.; Back, S.; Lee, J. H.; Choi, S. H.; Jung, Y.; Choi, J. W.; Mixed Transition Metal Oxide with Vacancy-Induced Lattice Distortion for Enhanced Catalytic Activity of Oxygen Evolution Reaction. *ACS Catal.* **2019**, *9*, 7099−7108.

(166) Liu, S. L.; Mu, X. Q.; Li, W. Q.; Lv, M.; Chen, Y. B.; Chen, C. Y.; Mu, S. C. Cation vacancy-modulated PtPdRuTe five-fold twinned nanomaterial for catalyzing hydrogen evolution reaction. *Nano Energy* **2019**, *61*, 346−351.

(167) Xu, K.; Sun, Y. Q.; Li, X. L.; Zhao, Z. H.; Zhang, Y. Q.; Li, C. C.; Fan, H. J. Fluorine-Induced Dual Defects in Cobalt Phosphide Nanosheets Enhance Hydrogen Evolution Reaction Activity. *ACS Materials Lett.* **2020**, *2*, 736−743.

(168) Zhou, P.; Wang, Y. Y.; Xie, C.; Chen, C.; Liu, H. W.; Chen, R.; Huo, J.; Wang, S. Y. Acid-etched layered double hydroxides with rich defects for enhancing the oxygen evolution reaction. *Chem. Commun.* **2017**, *53*, 11778−11781.

(169) Wang, Y. Y.; Zhang, Y. Q.; Liu, Z. J.; Xie, C.; Feng, S.; Liu, D. D.; Shao, M. F.; Wang, S. Y. Layered double hydroxide nanosheets with multiple vacancies obtained by dry exfoliation as highly efficient oxygen evolution electrocatalysts. *Angew. Chem. Int. Ed.* **2017**, *56*, 5867−5871.

(170) Liu, R.; Wang, Y. Y.; Liu, D. D.; Zou, Y. Q.; Wang, S. Y. Water-Plasma-Enabled Exfoliation of Ultrathin Layered Double Hydroxide Nanosheets with Multivacancies for Water Oxidation. *Adv. Mater.* **2017**, *29*, 1701546.

(171) Yuan, Z. J.; Bak, S. M.; Li, P. S.; Jia, Y.; Zheng, Li, R.; Zhou, Y.; Bai, L.; Hu, E. Y.; Yang, X. Q.; Cai, Z.; Sun, Y. M.; Sun, X. M. Activating Layered Double Hydroxide with Multivacancies by Memory Effect for Energy-Efficient Hydrogen Production at Neutral pH. *ACS Energy Lett*. **2019**, *4*, 1412−1418.

(172) Klein, J.; Engstfeld, A. K.; Brimaud, S.; Behm, R. J. Pt nanocluster size effects in the hydrogen evolution reaction: approaching the theoretical maximum activity. Phys. *Chem. Chem. Phys.* **2020**, *22*, 19059−19068.

(173) Zhou, S. M.; Miao, X. B.; Zhao, X.; Ma, C.; Qiu, Y. H.; Hu, Z. P.; Zhao, J. Y.; Shi, L.; Zeng, J. Engineering electrocatalytic activity in nanosized perovskite cobaltite through surface spin-state transition. *Nat. Commun*. **2016**, *7*, 11510.

(174) Zhou, M.; Bao, S. J.; Bard, A. J. Probing size and substrate effects on the hydrogen evolution reaction by single isolated Pt atoms, atomic clusters, and nanoparticles. *J. Am. Chem. Soc.* **2019**, *141*, 7327−7332.

(175) Li, T. F.; Liu, J. J.; Song, Y.; Wang, F. Photochemical solid-phase synthesis of platinum single atoms on nitrogen-doped carbon with high loading as bifunctional catalysts for hydrogen evolution and oxygen reduction reactions. *ACS Catal.* **2018**, *8*, 8450−8458.

(176) Zhu, H.; Gao, G. H.; Du, M. L.; Zhou, J. H.; Wang, K.; Wu, W. B.; Chen, X.; Li, Y.; Ma, P. M.; Dong, W. F.; Duan, F.; Chen, M. Q.; Wu, G. M.; Wu, J. D.; Yang, H. T.; Guo, S. J. Atomic-Scale Core/Shell Structure Engineering Induces Precise Tensile

Strain to Boost Hydrogen Evolution Catalysis. *Adv. Mater.* **2018**, *30*, 1707301.

(177) Meng, G.; Sun, W. M.; Mon, A. A.; Wu, X.; Xia, L. Y.; Han, A. J.; Wang, Y.; Zhuang, Z. B.; Liu, J. F.; Wang, D. S.; Li, Y. D. Strain Regulation to Optimize the Acidic Water Oxidation Performance of Atomic-Layer IrO_x. *Adv. Mater.* **2019**, *31*, 1903616.

(178) Zhou, D. J.; Wang, S. Y.; Jia, Y.; Xiong, X. Y.; Yang, H. B.; Liu, S.; Tang, J. L.; Zhang, J. M.; Liu, D.; Zheng, L. R.; Kuang, Y.; Sun, X. M.; Liu, B. NiFe hydroxide lattice tensile strain: enhancement of adsorption of oxygenated intermediates for efficient water oxidation catalysis. *Angew. Chem. Int. Ed.* **2019**, *58*, 736−740.

(179) Cheng, W. R.; Zhao, X.; Su, H.; Tang, F. M.; Che, W.; Zhang, Hui.; Liu. Q. H. Lattice-strained metal–organic-framework arrays for bifunctional oxygen electrocatalysis. *Nat. Energy* **2019**, *4*, 115−122.

(180) Sun, Y. F.; Gao, S.; Lei, F. C.; Liu, J. W.; Liang L.; Xie, Y. Atomically-thin non-layered cobalt oxide porous sheets for highly efficient oxygen evolving electrocatalysts. *Chem. Sci.* **2014**, *5*, 3976−3982.

(181) Chen, J. Y.; Cui, P. X.; Zhao, G. Q.; Rui, K.; Lao, M. M.; Chen, Y. P.; Zheng, X. S.; Jiang, Y. Z.; Pan, H. G.; Dou, S. X.; Sun, W. P. Low-Coordinate Iridium Oxide Confined on Graphitic Carbon Nitride for Highly Efficient Oxygen Evolution. *Angew. Chem. Int. Ed.* **2019**, *58*, 12540−12544.

(182) Fei, H. L.; Dong, J. C.; Feng, Y. X.; Allen, C. S.; Wan, C. Z.; Volosskiy, B.; Li, M. F.; Zhao, Z. P.; Wang, Y. L.; Sun, H. T.; An, P. F.; Chen, W. X.; Guo, Z. Y.; Lee, C.; Chen, D. L.; Shakir, I.; Liu, M. J.; Hu, T. D.; Li, Y. D.; Kirkland, A. I.; Duan, X. F.; Huang, Y. General Synthesis and Definitive Structural Identification of MN_4C_4 Single Atom Catalysts with Tunable Electrocatalytic Activities. *Nat. Catal.* **2018**, *1*, 63−72.

(183) Cao, L. L.; Luo, Q. Q.; Liu, W.; Lin, Y. K.; Liu, X. K.; Cao, Y. J.; Zhang, W.; Wu, Y.; Yang, J. L.; Yao, T.; Wei, S. Q. Identification of Single-Atom Active Sites in Carbon-Based Cobalt Catalysts During Electrocatalytic Hydrogen Evolution. *Nat. Catal.* **2019**, *2*, 134−141.

(184) Sa, Y. J.; Park, S. O.; Jung, G. Y.; Shin, T. J.; Jeong, H. Y.; Kwak, S. K.; Joo, S. H. Heterogeneous Co-N/C Electrocatalysts with Controlled Cobalt Site Densities for the Hydrogen Evolution Reaction: Structure-Activity Correlations and Kinetic Insights. *ACS Catal.* **2019**, *9*, 83−97.

(185) Huang, J. B.; Jiang, Y.; An, T. Y.; Cao, M. H. Increasing the active sites and intrinsic activity of transition metal chalcogenide electrocatalysts for enhanced water splitting. *J. Mater. Chem. A* **2020**, *8*, 25465−25498.

(186) Suen, N. T.; Hung, S. F.; Quan, Q.; Zhang, N.; Xu, Y. J.; Chen, H. M. Electrocatalysis for the Oxygen Evolution Reaction: Recent Development and Future Perspectives. *Chem. Soc. Rev.* **2017**, *46*, 337−365.

(187) Liu, X.; Jiao, Y.; Zheng, Y.; Davey, K.; Qiao, S. Z. A Computational Study on Pt, Ru Dimer Supported on Graphene for Hydrogen Evolution Reaction: New Insight into the Alkaline Mechanism. *J. Mater. Chem. A* **2019**, *7*, 3648−3654.

(188) Shi, Q.; Zhu, C.; Du, D.; Lin, Y. Robust Noble Metal-Based Electrocatalysts for Oxygen Evolution Reaction. *Chem. Soc. Rev.* **2019**, *48*, 3181−3192.

(189) Abruña, H. D.; White, J. H.; Albarelli, M. J.; Bommarito, G. M.; Bedzyk, M. J.; McMillan, M. Is There Any Beam Yet? Uses of Synchrotron Radiation in the in Situ Study of Electrochemical Interfaces. *J. Phys. Chem.* **1988**, *92*, 7045−7052.

(190) Weckhuysen, B. M. Snapshots of a Working Catalyst: Possibilities and Limitations of In Situ Spectroscopy in the Field of Heterogeneous Catalysis. *Chem. Commun.* **2002**, *2*, 97−110.

(191) Kanan, M. W.; Yano, J.; Surendranath, Y.; Dincá, M.; Yachandra, V. K.; Nocera, D. G. Structure and Valency of a Cobalt-Phosphate Water Oxidation Catalyst Determined by in Situ X-ray Spectroscopy. *J. Am. Chem. Soc.* **2010**, *132*, 13692−13701.

(192) Risch, M.; Stoerzinger, K. A.; Han, B.; Regier, T. Z.; Peak, D.; Sayed, Y.; Wei, C.; Xu, Z.; Shao-Horn, Y. Redox Processes of Manganese Oxide in Catalyzing Oxygen Evolution and Reduction: An in Situ Soft X-Ray Absorption Spectroscopy Study. *J.*

Phys. Chem. C **2017**, *121*, 17682−17692.

(193) Friebel, D.; Viswanathan, V.; Miller, D. J.; Anniyev, T.; Ogasawara, H.; Larsen, A. H.; O'Grady, C. P.; Nørskov, J. K.; Nilsson, A. Balance of Nanostructure and Bimetallic Interactions in Pt Model Fuel Cell Catalysts: In Situ XAS and DFT Study. *J. Am. Chem. Soc.* **2012**, *134*, 9664−9671.

(194) Yang, Y.; Xiong, Y.; Zeng, R.; Lu, X. Y.; Krumov, M.; Huang, X.; Xu, W. X.; Wang, H. S.; DiSalvo, F. J.; Brock, J. D.; Muller, D. A.; Abruña, H. D. Operando Methods in Electrocatalysis. *ACS Catal.* **2021**, *11*, 1136−1178.

(195) Wang, H. Y.; Hsu, Y. Y.; Chen, R.; Chan, T. S.; Chen, H. M.; Liu, B. Ni^{3+}-Induced Formation of Active NiOOH on the Spinel Ni–Co Oxide Surface for Efficient Oxygen Evolution Reaction. *Adv. Energy Mater.* **2015**, *5*, 1500091.

(196) Jiang, J.; Sun, F. F.; Zhou, S.; Hu, W.; Zhang, H.; Dong, J. C.; Jiang, Z.; Zhao, J. J.; Li, F. F.; Yan, W. S.; Wang, W. Atomic-level insight into super-efficient electrocatalytic oxygen evolution on iron and vanadium co-doped nickel (oxy)hydroxide. *Nat. Commun.* **2018**, *9*, 2885.

(197) Povia, M.; Abbott, D. F.; Herranz, J.; Heinritz, A.; Lebedev, D.; Kim, B.-J.; Fabbri, E.; Patru, A.; Kohlbrecher, J.; Schäublin, R.; Nachtegaal, M.; Copéret, C.; Schmidt, T. J. Operando X-ray characterization of high surface area iridium oxides to decouple their activity losses for the oxygen evolution reaction. *Energy Environ. Sci.* **2019**, *12*, 3038−3052.

(198) Hu, Q.; Liu, X.; Zhu, B.; Fan, L.; Chai, X.; Zhang, Q.; Liu, J.; He, C.; Lin, Z. Crafting MoC_2-Doped Bimetallic Alloy Nanoparticles Encapsulated within N-Doped Graphene as Roust Bifunctional Electrocatalysts for Overall Water Splitting. *Nano Energy* **2018**, *50*, 212−219.

(199) Li, L.; Wang, P.; Shao, Q.; Huang, X. Metallic Nanostructures with Low Dimensionality for Electrochemical Water Splitting. *Chem. Soc. Rev.* **2020**, *49*, 3072−3106.

(200) Zhang, J. Y.; Xiao, W.; Xi, P. X.; Xi, S. B.; Du, Y. H.; Gao, D. Q.; Ding, J. Activating and Optimizing Activity of CoS_2 for Hydrogen Evolution Reaction through the Synergic Effect of N Dopants and S Vacancies. *ACS Energy Lett.* **2017**, *2*, 1022−1028.

(201) Li, R.-Q.; Hu, P.; Miao, M.; Li, Y.; Jiang, X.-F.; Wu, Q.; Meng, Z.; Hu, Z.; Bando, Y.; Wang, X.-B. CoO-modified Co_4N as A Heterostructured Electrocatalyst for Highly Efficient Overall Water Splitting in Neutral Media. *J. Mater. Chem. A* **2018**, *6*, 24767−24772.

(202) Yuan, X. T.; Ge, H. X.; Wang, X.; Dong, C. L.; Dong, W. J.; Riaz, M. S.; Xu, Z. W.; Zhang, J. X.; Huang, F. Q. Controlled Phase Evolution from Co Nanochains to CoO Nanocubes and Their Application as OER Catalysts. *ACS Energy Lett.* **2017**, *2*, 1208−1213.

(203) Li, W.; Niu, Y. L.; Wu, X. J.; Wu, F. W.; Li, T. H.; Hu, W. H. Heterostructured $CoSe_2$/$FeSe_2$ Nanoparticles with Abundant Vacancies and Strong Electronic Coupling Supported on Carbon Nanorods for Oxygen Evolution Electrocatalysis. *ACS Sustainable Chem. Eng.* **2020**, *8*, 4658−4666.

(204) Zhou, X.; Gao, H.; Wang, Y.; Liu, Z.; Lin, J.; Ding, Y. P vacancies-enriched 3D hierarchical reduced cobalt phosphide as a precursor template for defect engineering for efficient water oxidation. *J. Mater. Chem. A* **2018**, *6*, 14939−14948.

(205) Zhou, Y.; Fan, H. J. Progress and Challenge of Amorphous Catalysts for Electrochemical Water Splitting. *ACS Materials Lett.* **2021**, *3*, 136−147.

TOC Figure

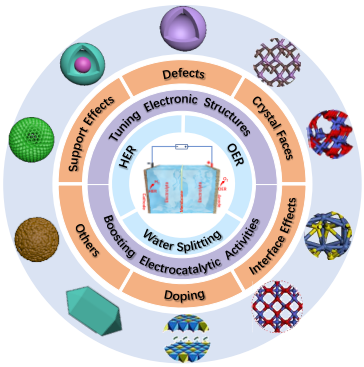
Defects
Crystal Faces
Interface Effects
Doping
Others
Support Effects
Tuning Electronic Structures
HER
OER
Water Splitting
Boosting Electrocatalytic Activities